Supplementary Materials

Endocytosis caused by liquid-liquid phase separation of proteins

Louis-Philippe Bergeron-Sandoval[1], Hossein Khadivi Heris[2], Adam G. Hendricks[2], Allen J. Ehrlicher[2], Paul François[3], Rohit V. Pappu[4] and Stephen W. Michnick[1,5*]

correspondence to: S.W.M. (stephen.michnick@umontreal.ca).

This PDF file includes:

Materials and Methods

Figures S1 to S15

Tables S1 to S4

Captions for Movies S1

References

Other Supplementary Materials for this manuscript includes the following:

Movies S1

Materials and Methods:

Cell culture, gene manipulations and fluorescent reporters

We performed *in vivo* experiments in the *Saccharomyces cerevisiae* BY4741 *MATa his3Δ1 leu2Δ0 met15Δ0 ura3Δ0* background. Cells were normally grown to exponential phase (OD$_{600}$ 0.1 to 0.6) in either rich medium (YPD) or low fluorescence medium (LFM) . Liquid media or solid-agar cultures were incubated at 30°C. To decouple the effects of turgor pressure on clathrin-mediated endocytosis (CME) we performed many experiments in a yeast strain with the gene for glycerol-3-phosphate dehydrogenase deleted, *GPD1Δ*. We acquired the *GPD1Δ* and other deletion strains from the Yeast Knock-out (YKO) deletion collection and GFP fluorescent strains from the Yeast GFP Clone Collection (Huh, Falvo et al. 2003), were generous gifts from J Vogel at McGill University.

For 2-color imaging and other specific needs, the coding sequences for different fluorescent proteins were integrated into the genome, 3' to reporter protein open reading frames (ORFs) by homologous recombination (Tarassov, Messier et al. 2008). In short, mCherry, Dronpa3 and Venus tags were integrated *via* homologous recombination by amplifying the HPH or NAT resistance cassettes from the respective pAG32 or pAG25 vectors with primer tails homologous to flanking sequences to the respective loci. BY4741, *GPD1Δ* or other YKO strains were then transformed with the respective PCR cassettes, selected for HPH or NAT resistance in YPD medium and confirmed by diagnostic PCR.

Truncation and site-directed mutagenesis within ORFs

Integration of the coding sequence for fluorescent protein Venus YFP by homologous recombination into the genome was also used to truncate the prion-like domains (PLDs) sequences in the ORFs of Sla1, Ent1, Ent2, Yap1801 and Yap1802. In order to truncate the required gene fragments, the Venus YFP coding sequence was integrated at precise locations prior to the STOP codon. The amino acid sequences that are deleted in each PLD truncation mutant are; Sla1 (1170-1245Δ), Ent1 (214-455Δ), Ent2 (255-615Δ), Yap1801 (355-630Δ) and Yap1802 (321-569Δ).

To generate proline substitution point mutations within or near PLDs of Sla1 and Ent2; we cloned synthetic gene fragments (GenScript) that coded for the mutations into the respective MoBy-ORF p5472 plasmids of our target genes (Ho, Magtanong et al. 2009). The respective position of proline mutations, gene fragment size and restriction enzymes are; Sla1 G1224P, Q1227P, A1231P, F1234P (842 bp, NarI and XmaI); Ent2 R359P, Q362P, H366P, L369P, L385P, L388P, K401P, E404P, L408P, Q411P, L415P, Q418P (1395 bp, XhoI and AflII). Standard cloning procedures with matching restriction enzymes were used to build the constructs and we confirmed final constructs by sequencing. Respective deletion strains were then complemented with either the proline-mutated or original p5472 plasmids.

Diffraction-limited fluorescence microscopy

For most experiments, cells were grown in LFM to an OD_{600} of ~0.1 to 0.6 and plated on either Nunc glass bottom 96-well plates (Thermo Scientific; 164588), glass bottom 8-well plates (Ibidi) or glass bottom 35 mm round dishes (MatTek). We used concanavalin A (Sigma-Aldrich ConA # C-7275) as a cell surface binding agent. Each well was loaded with 1mg/ml final concentration of ConA solution at room temperature for 15 minutes. ConA was then removed and wells were completely air dried before cells were added. Fluorescence images were acquired with distinct imaging platforms;

For the assessment of PLD truncations, we imaged cells on a Nikon TE2000 inverted microscope equipped with a 100X/1.45 plan APO lambda oil objective (Nikon), X-Cite lamp source (Excelitas), respective FITC (Chroma 41001HQ), EYFP (Chroma 49003ET) and mCH/TR (Chroma 49008ET) dichroic cubes and a Cool SNAP HQ camera. Z-stacks were acquired through a micron deep region with 5 planes and presented by maximal Z-projection.

For the measurements of fluorescent probe uptake and cell sizes under different osmotic pressures, fluorescence images were collected on an InCell 6000 automated confocal microscope configured with a 100x/0.9 Plan FLUOR objective (Nikon) and 488 nm laser diode and FITC 525/20 emission filter for GFP fluorescence or 561 nm DPSS laser and dsRed 605/52 emission filter (GE healthcare life sciences). Single or two color images were collected sequentially on a single focal plane with an exposure time of 100 msec. and a confocal slit of 2 AU. Image analysis and signal automated segmentation was performed with the InCell Developer software (GE healthcare life sciences) and the data was further analyzed and plotted in the R environment.

For other imaging data, the Quorum Diskovery platform was used in open aperture, confocal and super-resolution imaging modes. Our Quorum Diskovery platform consists of a Leica DMi6000 inverted microscope equipped with a Diskovery multi-modal imaging system (Spectral) attached to either a Hamamatsu EM X2 camera or ORCA FLASH 4.0 V2 digital CMOS camera. Wide field or confocal excitation are achieved with a Spectral laser merge module with mounted 405 nm, 440 nm, 488 nm, 561 nm, and 640 nm diode pumped solid state laser sources linked to a Borealis beam conditioning unit. Images were acquired with a HCX PL APO 63x /1.47 NA oil corrected TIRF objective (Leica). This platform was remote controlled by the Metamorph software (Molecular Devices) and images were acquired and analyzed trough distinct pipelines. For particle tracking and mean squared displacement analyses, we used the Wave Tracer plugin to localize fluorescent foci centroid position through a wavelet algorithm and tracks particles in times stacks to calculate particles movement.

Finally, a Axio Imager Z2 spinning disk confocal microscope with a DirectFRAP module (Carl Zeiss) was used for all the FRAP assays. Complete details of FRAP experiments are included below. This imaging platform is equipped with a AxioCam mRM charged-coupled device camera (Carl Zeiss), a DirectFRAP module (Carl Zeiss) and filter sets 49002 ET-GFP and 49008 ET-mCherry from Chroma Technology.

Fluorescent probes to quantify endocytosis or detect amyloid structures

Lucifer yellow (LY; Molecular Probes) assays to quantify endocytosis were performed at a final concentration of 1 mg/ml in YPD medium. Cells were incubated with the LY for 20 min or more. We then centrifuged at 3000 x g and washed cells 3 times in phosphate buffered saline (PBS; 137 mM sodium chloride, 10 mM phosphate, 2.7mM potassium chloride) before imaging in either PBS or LFM with excitation wavelength (λ_{ex}) of 428 nm and emission wavelength (λ_{em}) of 536 nm.

The lipophlic stryryl dye FM4-64 (*N*- (3-Triethylammoniumpropyl)-4- (6- (4- (Diethylamino) Phenyl) Hexatrienyl) Pyridinium Dibromide) (Molecular Probes) was used to monitor plasma membrane uptake and staining of vacuolar membranes. Plasma membrane was labeled with 10 to 20 µM FM4-64 in YPD media and cells were incubated for 5 to 120 min. Cells were washed once in PBS and resuspended in LFM for imaging. FM4-64 stained cells were quantified by fluorescence microscopy (λ_{ex} of 510 nm, λ_{em} of 750 nm) on our Quorum platform or if specifically indicated on the InCell6000 (see Diffraction-limited fluorescence microscopy section). When cell populations (or conditions) were compared, we applied a Welch's two-sided t-test with sample sizes to achieve a power greater than 0.9 with a 95% confidence level.

We determined whether Sla1-mCherry puncta were also labeled with the amyloid binding dye thioflavin T (ThT) in both live and fixed cells. Live cell ThT staining was performed as described by Kroschwald and collaborators (Kroschwald, Maharana et al. 2015). Cells grown to OD_{600} ~0.6 were harvested and resuspended in 30 µM ThT, 10 mM Tris/EDTA buffer (pH 7) for 20 min. Cells were then washed 3 times in PBS and resuspended in LFM media for imaging. Fluorescence microscopy (λ_{ex} of 405nm, λ_{em} of 450/50 nm) or (λ_{ex} of 488 nm, λ_{em} of 525/50 nm) were performed on the Quorum platform (see Diffraction-limited fluorescence microscopy section). BY4741 cells transformed with the plasmid pRS416-GAL-Sup35NM-RFP and induced for 2 hours in 2% galactose LFM were used as positive ThT stain controls. Alternatively, we confirmed ThT *in vivo* results with ThT staining of fixed cells. Cells were fixed with 4% paraformaldehyde 2% sucrose PBS for 20 min and washed once in PBS. Cells were then permeabilized with 0.1% Triton-X phosphate buffered (pH 7.5) detergent solution, and treated with 0.001% ThT for 10 min at room temperature. ThT stained cells were washed at 3–4 times with PBS and imaged on the Quorum platform (λ_{ex} of 488 nm, λ_{em} of 525/50 nm) (see Diffraction-limited fluorescence microscopy section).

Cell treatment with water-glycerol solutions, 1,6 hexanediol and latrunculin-A

Water and glycerol binary combinations were mixed to obtain solutions with precise osmotic pressures ranging from 1.4 MPa to 30 MPa. Cells were grown to log phase, centrifuged for 2 minutes at 3000 x g and resuspended in the different water-glycerol binary solutions in Nunc 96-well glass bottom imaging plates (Thermo Scientific; 164588). Fluorescence images of cells, that express EGFP from a pAG416-GPD plasmid, were then captured immediately after resuspension and at 1 hour intervals with the confocal InCell6000 (see Diffraction-limited fluorescence microscopy section). Intensity thresholding of the GFP channel allowed us to segment the cells

and obtain cell area values. These area values were used as a proxy for cell size at the different osmotic pressures.

We utilized 1,6-hexanediol (HD) to differentiate phase separated intracellular bodies from stable solid or fibrillar protein aggregates or to modulate the interactions among proteins that compose the cortical droplet. HD is thought to change the solvent quality inside cells resulting in disruption of the interactions favorable to liquid-liquid phase separation. 1,2,3-hexanetriol (HT) was used as a negative control in all the HD assays. We treated cells grown to mid-log phase (OD_{600} 0.6) with HD or HT from 0 to 10 % wt/v and we measured both the uptake of fluorescent probes and progression of CME protein accumulation at cortical foci by fluorescence microscopy. Lifetime of Sla1-GFP at cortical sites in the presence of HD was assessed on the Quorum platform (see Diffraction-limited fluorescence microscopy section) and kymographs were generated with the Metamorph image analysis software (Molecular Devices).

Inhibition of F-actin synthesis was achieved using Latrunculin A (LatA) at concentrations determined by titrating LatA from 0 to 50 µM. Cells were treated for 20 minutes prior to measurements of the uptake of membrane (FM6-64 dye) and bulk fluorescent reporter uptake (LY dye) and of Abp1-mCherry accumulation at cortical foci described above for the HD assays. The dose-response curve indicated that a concentration of 20 µM LatA was sufficient to impair actin nucleation at cortical sites and we used this concentration of LatA in all our experiments unless mentioned otherwise.

Direct stochastic optical reconstruction microscopy (dSTORM)

Direct stochastic optical reconstruction data was acquired with the custom-imaging platform built by Quorum Technologies (see Diffraction-limited fluorescence microscopy section). Sample preparation for dSTORM was performed according to Reiter, *et al.* with minor modifications (Reiter, Anrather et al. 2012). Cells were grown to an OD_{600}= 0.1 and plated on ConA coated glass bottom 35 mm round dishes for 10 minutes. Cells were then fixed with 4 % paraformaldehyde 2% sucrose PBS for 15 min. Fixation was stopped with two sequential incubations of 10 minutes in 50 mM NH_4Cl PBS and cells were further permeabilized and blocked in 0.25 % Triton X-100, 5 % BSA, 0.004 % NaN_3 PBS for another 30 minutes. We used GFP-trap nanobodies (Chromotek) to label Sla1-GFP at a concentration of 10 µM in 0.25 % Triton X-100, 1% BSA, 0.004 % NaN_3 PBS for 60 minutes. Cells were washed extensively in PBS before imaging in blinking buffer 30 mM β-mercaptoethylamine (MEA), 0.5 % glucose, 0.25 mg/ml glucose oxidase and 20 µM catalase. We acquired streams of 10,000 to 20,000 frames at 30 msec. exposures and we used Wave Tracer plugin (Molecular Devices) to detect and gate events with a 16-bit intensity threshold of 1,000. When possible we didn't use gain on the EMCCD camera to better calculate resolution; the camera has a conversion factor of $6e^-$/count when no gain is used. Based on photon counts, we estimate an x, y-resolution of ≈10 nm with the 647 nm wavelength Alexa-647 fluorophore and a z-resolution of ≈50 nm with the astigmatic lens in 3D configuration calibrated on TetraSpeck beads (ThermoFisher). Center of mass for each event was calculated and we reconstructed images in Wave Tracer before further

analysis in Metamorph (Molecular Devices). Sla1 structures were separated in circular and narrow elliptical shapes that correspond respectively to structure within or at the equator of cells.

Fluorescence recovery after photobleaching

Fluorescence recovery after photobleaching (FRAP) experiments (for recovery of Sla2-GFP and dextran-FITC) were performed on a Axio Imager Z2 spinning disk confocal microscope (Carl Zeiss). Images were acquired with a 100x NA 1.3 oil objective and a circular FRAP ROI-size of 1.5 µm of diameter selected from the DirectFRAP diaphragm wheel. A photobleaching 488 nm 100 mW laser unit was pulsed for 1 second on samples, followed by acquisition of fluorescence recovery with time resolution from 50 msec. to 2 seconds depending on samples. Analysis of the images intensity (I) fluctuations and segmentation of regions of interest (ROI) were performed on Zen imaging software (Carl Zeiss). We analyzed the data as follows:

We first determined bleach depth with the equation:

$$bleach\ depth = \frac{\left(\frac{1}{n_{pre}} \cdot \sum_{t=1}^{n_{pre}} I\ (t)_{ROI\ 1'}\right) - I\ (t)_{ROI\ 1'}}{\frac{1}{n_{pre}} \cdot \sum_{t=1}^{n_{pre}} I\ (t)_{ROI\ 1'}} ; \qquad (1.1)$$

, and then applied a double normalization on bleached ROI1:

$$I\ (t)_{dbl\ norm} = \left(\frac{\frac{1}{n_{pre}} \cdot \sum_{t=1}^{n_{pre}} I\ (t)_{ROI\ 2'}}{I\ (t)_{ROI\ 2'}}\right) \cdot \left(\frac{I(t)_{ROI\ 1'}}{\frac{1}{n_{pre}} \cdot \sum_{t=1}^{n_{pre}} I(t)_{ROI\ 1'}}\right) ; \qquad (1.2)$$

, where ROI2 is a non-bleached region and n_{pre} is the number of pre-bleached images. We finally fitted each normalized trace with a non-least square function to best fit the single term equation:

$$f(I) = I_0 - a \cdot e^{-\omega t} ; \qquad (1.3)$$

from which we extracted half recovery times for the Sla2-GFP and dextran-FITC samples. We selected the Sla2 protein because the apparent number of molecule in the fluorescent foci remains relatively constant during vesicle budding (Picco, Mund et al. 2015). We nonetheless corrected for possible accumulation or reduction of the total number of molecules in the foci with a rate of 4 molecules per second in the initial or the last 5 seconds of the acquired recovery window. Analyses were performed using subroutines of the R package.

Centroid tracking of Sla1 foci

We measured the mean square displacement (MSD) of single Sla1-GFP fluorescent foci within a confocal volume on the Quorum platform (see Diffraction-limited fluorescence microscopy section). Images were acquired at 20 fps for 30 seconds with a 50 μm pinhole spinning disk and we performed particle centroid tracking with the Wave Tracer plugin in the Metamorph software (Molecular Devices). We included only foci that remained in the confocal volume throughout the acquisition and which showed decreasing fluorescence intensity as a function of MSD (Fig. S12a). We next determined the linear displacement of the Sla1 foci towards the cell interior with the particle coordinates plotted as a function of elapsed time (Fig. S12b).

Quantification of membrane in nascent vesicles under HD titration

We quantified the amount of membrane in single nascent CME vesicles by fluorescence emitted from FM6-64 labelled membrane. Overnight Sla1-YFP cell cultures were diluted 1:40 in fresh LFM with HD concentrations from 0 to 5%. Cells were incubated in the HD solutions for 5 minutes and then labelled with 5 μM FM4-64 for another 5 minutes before direct fluorescence image acquisition on the Quorum platform (see Diffraction-limited fluorescence microscopy section). Single vesicles where segmented with an intensity threshold in both YFP and FM4-64 channels to quantify the membrane fluorescence that co-localizes with Sla1 signal. Average intensity measurements per nascent vesicle were normalized to values between 0 and 1 for the whole HD treatment concentration range. As a reference point to compare with membrane invagination predictions, we extracted mean and standard deviation values from data for HD concentration below 2 %; mean and standard deviation were also determined for each HD concentration.

Effect of 1,6-hexanediol (HD) titration on droplet stability

Formation of a cortical droplet results in an interface between the droplet and the cytosol and we can treat the droplet and the dispersed cytosol as two phases defined by an interface between them. In a mean field description, the cohesive interactions that drive the formation of the droplet derive from the balance of interactions amongst the droplet and cytosolic components. This will determine the stability of the droplet. In addition, the interface between the droplet and cytosol will be governed by an interfacial tension. A simple adaptation of the Flory-Huggins model for binary mixtures can be used to quantify the interfacial tension (Dill and Bromberg 2011).

The model is as follows: We shall define two condensed phases *viz.*, the droplet phase (D) and the cytosolic phase (C). The interfacial tension γ_{DC} defines the free energy penalty associated with increasing the interfacial area between the two phases. If $\gamma_{DC} > 0$, then the interfacial area will be minimized, thus resulting in spherical droplets. From the vantage point of the droplet, reducing the interfacial tension decreases the number of droplet components that are "sacrificed" to be at the interface and thus lose favorable intra-droplet interactions.

If the total free energy of the two bulk phases D and C and the interface between the phases is F, then the interfacial tension associated with changing the interfacial area A is defined as:

$$\gamma_{DC} = \left(\frac{\partial F}{\partial A}\right)_{n_D, n_C, T} ; \qquad (2.1)$$

For simplicity, we shall use a mean-field model with the two phases defined on a lattice with coordination number z. The molecules of D and C will be assumed to be of similar size and the translational entropy will be set to zero. If a is the area per molecular unit that is exposed to the interface, then equation (2.1) becomes:

$$\gamma_{DC} = \left(\frac{\partial F}{\partial A}\right)_{n_D, n_C, T} = \left(\frac{\partial U}{\partial A}\right)_{n_D, n_C, T} = \frac{1}{a}\left(w_{DC} - \frac{w_{DD} + w_{CC}}{2}\right); \qquad (2.2)$$

Here, the w terms are the effective mean-field energies associated with interactions between components of the droplet (w_{DD}), the cytosol (w_{CC}) and the components of the droplet and the cytosol (w_{DC}). These energies are in units of k_BT and the convention is that the energies are negative if they are favorable and positive if they are unfavorable. Accordingly, it follows that:

$$\gamma_{DC} > 0 \text{ if } |w_{DC}| < \left|\frac{w_{DD} + w_{CC}}{2}\right|$$

$$\gamma_{DC} = 0 \text{ if } |w_{DC}| = \left|\frac{w_{DD} + w_{CC}}{2}\right|; \qquad (2.3)$$

$$\gamma_{DC} < 0 \text{ if } |w_{DC}| > \left|\frac{w_{DD} + w_{CC}}{2}\right|$$

Importantly, equation (2.2) can be rewritten in terms of the Flory-Huggins interaction coefficient using the relationship:

$$\chi_{DC} = \frac{z}{k_BT}\left[w_{DC} - \left(\frac{w_{DD} + w_{CC}}{2}\right)\right] = \left(\frac{c_E}{k_BT}\right); \qquad (2.4)$$

Here, c_E is cohesive energy that holds the droplet together and represents the balance of droplet-cytosol, intra-droplet and intra-cytosol interactions. Accordingly,

$$\gamma_{DC} = \frac{1}{a}\left(w_{DC} - \frac{w_{DD} + w_{CC}}{2}\right) = \left(\frac{k_BT}{za}\right)\chi_{DC};$$

$$za\gamma_{DC} = k_BT\chi_{DC} \qquad (2.5)$$

Alternatively,

$$\chi_{DC} = \left(\frac{za}{k_BT}\right)\gamma_{DC} = \left(\frac{c_E}{k_BT}\right); \qquad (2.6)$$

8

$$za = \left(\frac{c_E}{\gamma_{DC}} \right)_{HD=0\%} ; \qquad (2.7)$$

Note that the values of *z* and *a* are fixed by the lattice and components of the droplet. Through measurements combined with the Young-Laplace theory, we have estimates of the interfacial tension and c_E in the absence of HD – as shown in equation (2.7). These estimates can be used as shown in equation (2.7) to estimate the value of *za*. Since this value of *za* is independent of HD concentration, one can fix *za* and use the estimate of cohesive energy c_E at different HD concentrations to estimate the change in interfacial tension as a function of HD concentration using equation (2.8) below:

$$\gamma_{DC}\left(\%HD\right) = \left[\frac{c_E\left(\%HD\right)}{za} \right]; \qquad (2.8)$$

Polystyrene beads and Dextran-FITC osmoporation
To incorporate dextran-FITC of different chain length inside haploid yeast cells, we used an osmoporation technique similar to that described by da Silva Pedrini *et al.* (da Silva Pedrini, Dupont et al. 2014). Cells were centrifuged for 2 minutes at 3000 x g and resuspended in a water-glycerol binary solution at 1.4 MPa for 30 minutes, then in a 30 MPa solution for 1 hour. Osmoporation of dextran-FITC is performed after these steps, by centrifuging cells at 3000 x g and resuspending the pellet in the 1.4 MPa water-glycerol solution with the dextran-FITC at 10 mg/ml for 1h. After this incubation period, cells were put on ice and washed 3 times with cold PBS. Cells were preserved on ice until they were plated on ConA treated 35 mm imaging dishes for 10 minutes and imaged on either the Quorum or Zeiss platforms (see Diffraction-limited fluorescence microscopy section).
We also incorporated 200 nm orange (540/560) FluoSpheres carboxylate-modified polystyrene beads (ThermoFisher) with this technique. Beads where either coated with 10 mg/ml BSA or directly incorporated in strains with Sla2-Dronpa3 fluorescent protein. After osmoporation, cells were preserved on ice until they were plated on ConA treated coverslips and mounted on glass imaging slides for subsequent image acquisition and optical tweezers experiments.

microNS-GFP micro-rheology
To determine the effect of *osmoporation* on the cell rheological properties, we measured displacement of expressed viral capsid microNS particles labeled with GFP in both normal and osmoporated cells (Fig. S9). Cells were transformed with the microNS-GFP pRS expression plasmid, a generous gift of S. Alberti at Max Planck Institute of Molecular Cell Biology and Genetics (MPI-CBG). microNS movement was recorded on the Quorum platform (see Diffraction-limited fluorescence microscopy section) within a 2 micron thick Z-stack of 5 confocal planes (50 μm pinholes) acquired at 5 frames per second (fps). Image analysis was performed with Metamorph and Wave Tracer plugin (Molecular Devices), to track particles

displacement with centroid localization on maximum intensity projections. We further filtered the mean square displacement (MSD) data for particles that are confined and showed that they have MSD similar to the technical noise of our apparatus setup.

Optical tweezers measurements and calibration

Dynamic mechanical analysis of yeast cytoplasm was performed with a custom optical tweezers (OT) platform. Our OT system is an inverted microscope (Nikon Ti-E) equipped with a CFI APO SR TIRF 100x / 1.49 NA oil immersion objective (Nikon), a 1,064 nm Nd:YVO$_4$ 10 W infrared laser (IPG Photonics), an X-cite lamp source (Excelitas) and a nano-positioning stage (Mad City Labs). Oscillation of the tweezers on the specimen plane from 0.1 Hz to 2000 Hz was achieved with an acousto-optic deflector (AOD, AA Optoelectronics) coupled to a digital frequency synthesizer that we controlled with in house Labview routines. Light transmitted through the specimen was collected with a condenser lens and reflected onto a position-sensitive detector (PSD) (Thorlabs, PDP90A) to perform back focal plane interferometry. Before acquisitions we adjusted the microscope for Köhler illumination and ensured that all the optics were conjugate to the respective specimen plane or back focal plane. At each frequency of excitation we recorded the signals (120,000 samples at 1000 Hz to 2,000,000 samples at 0.1 Hz at 20 kHz) and performed Fourier analysis. Measurement time for each frequency sweep was about 15 minutes. For each sample, we covered the frequency domain from high-to-low frequencies, then we repeated the procedure from low-to-high to ensure consistent frequency response with prolonged laser exposure.

Calibration of the optical tweezers measures was performed as previously described with minor modifications (Hendricks, Holzbaur et al. 2012). Data analysis was conducted with in-house Matlab code. Data quality was first confirmed by assessment of the sinusoidal shape of the response to the applied stress. Traces with a coherence of 0.95 or greater were included in the analysis. We averaged 17 traces in distinct cellular locations and determined their trap stiffness k_{trap} (mean ± standard error; 8.0 x 10^{-5} ± 2.7 x 10^{-5} N•m^{-1}), photodiode sensitivity factor β (mean ± standard error 10.7 x 10^{3} ± 2.3 x 10^{3} nm•V^{-1}) and frequency-dependent viscoelastic moduli G' (storage) and G'' (loss) (see Fig. 3).

To account for the relaxation dynamics observed, we performed a fit on the forced response to sinusoidal oscillations and the power spectra of the spontaneous fluctuations of the bead to a model of a crosslinked network of flexible polymers (Lieleg, Schmoller et al. 2009) .

$$G' = G_0 - a \cdot \frac{N k_{off}}{\frac{k_{off}^2}{4\pi^2} + f^2} + b \cdot \left(\frac{f}{f_0}\right)^\alpha ; \qquad (2.9)$$

$$G'' = c \cdot \frac{Nf}{\frac{k_{off}^2}{4\pi^2} + f^2} + d \cdot \left(\frac{f}{f_0}\right)^{\alpha} ; \qquad (2.10)$$

From these fits, we extracted the average parameters (G_0; 16.53), (f_0; 37.44), number of crosslinks (N; 3×10^{14}), crosslink off-rate (k_{off}; 8.28), power law (α; 0.98) and constants ratios (a/b; 1.06×10^{-14}/2.19), (c/d; 1.33×10^{-14}/0.72). Deviation of α above a value 0.75 indicates that retraction or extension of entangled protein filaments ends could contribute to the relaxation mechanism (Koenderink, Atakhorrami et al. 2006).

Dimensions and geometry of membrane contour and cortical droplets
From published EM data, we considered that the optimal membrane U-shaped geometry before vesicle excision is about 70 nm high and 60 nm wide (Idrissi, Grotsch et al. 2008, Kukulski, Schorb et al. 2012). To approximate the area and volume, the U-shape was decomposed into a hemispherical cap of 30 nm radius over a cylinder of 30 nm radius and 40 nm high. We then calculated, with these dimensions, an invaginated membrane area of 1.32×10^{-14} m^2 and volume of 1.70×10^{-22} m^3.
We also defined for the membrane bending energy, the invagination height profile as a function of position around the invagination peak and middle of the droplet;

$$h(x,y) = h_0 \cdot \exp\left(\frac{-(x^2 + y^2)}{2R_0^2}\right) ; \qquad (3.1)$$

where h_0 is the invagination depth and R_0 is the radius of invagination.
To calculate the area and volume occupied by the cortical droplet and thus the amount of displaced cytosol material, we used our dSTORM measurements. The hemispherical cortical droplet volume was calculated to be 2.43×10^{-21} m^3 for a radius of 105 nm. The same hemispheric droplet has an area of 6.93×10^{-14} m^2. These dimensions agree with the size of ribosome exclusion zones observed surrounding invaginated clathin patches observed by EM (Kukulski, Schorb et al. 2012).

Calculation of the energies that counteract membrane invagination
Our observation of cortical droplets coupled to endocytosis suggests that membrane deformation in actin-independent CME results from a droplet-dependent stress. It has been proposed that some contribution to the energy needed for membrane invagination in CME could be provided by the clathrin lattice, by membrane-curving convex-shaped BAR domains (for Bin, Amphiphysin and Rvs) in BAR domain-containing proteins, insertion of amphipathic protein helix into membrane layers (Ford, Mills et al. 2002), lipid composition or simply by steric exclusion or crowding of proteins at cortical sites. It's also possible that alternative mechanisms

have an additive effect *in vivo*, but the mechanism we introduce here is essential to actin-independent membrane invagination. We examined each of these arguments in turn.

Although clathrin forms a cage structure around mature endosomes it was recently demonstrated that it assembles into a flat lattice on cortical sites (Avinoam, Schorb et al. 2015). Furthermore, studies have showed that clathrin doesn't produce work or curve the membrane itself (Idrissi, Blasco et al. 2012). Deletion of clathrin heavy chain gene (*CHC1Δ*) does not change the morphology or the rate of formation of CME vesicles (Kukulski, Picco et al. 2016). Clathrin, thus, may provide a scaffold for binding of other proteins involved in CME, be essential to site selection, and participate in vesicle size and scission (Kukulski, Picco et al. 2016).

Second, proteins containing BAR domains, that have a curved structure, have been implicated in membrane remodeling, including in the scission step of CME that requires the BAR domain-containing proteins Rvs161 and Rvs167 (Youn, Friesen et al. 2010). The only protein, however, that contains a BAR domain that is recruited to CME nucleation site prior to actin synthesis is Syp1 (Fig. S1). As previously reported deletion of the BAR domain of Syp1 had no effect on CME. Our results exclude a role of Syp1 F-BAR domain in inducing membrane curvature but not in other functions including to act as a sensor of membrane curvature (Boettner, D'Agostino et al. 2009), forming membrane microdomains (French, Zhao et al. 2013) or polarizing CME cortical sites in the cell (Kanshin, Bergeron-Sandoval et al. 2015).

Third, simple steric repulsion of proteins bound to and concentrated at confined membrane surfaces were proposed to cause invaginations of membranes *in vivo* and *in vitro*, including proteins implicated in CME. The disordered C-terminal domains (CTDs) of to Ent1/2 and Yap1801/1802 proteins can crowd membranes and induce tubulation of giant unilamellar vesicles (GUVs). They further propose an in vivo model, where Epsin1 and Ap180 disordered CTDs create *steric pressure* at the intracellular surface that increases the membrane curvature. Furthermore, Gleisner and collaborators recently demonstrated the ability of these ENTH proteins to effectively reduce membrane tension of GUVs, thus facilitating deformation and curvature of the membrane (Busch, Houser et al. 2015, Gleisner, Kroppen et al. 2016). The precise physical mechanisms by which Epsins and protein crowding in general drives membrane invagination *in vivo* is unclear. As we describe in our work, however, the geometries of the hemispherical body composed of CME coat proteins and that of the membrane invagination are not consistent with those expected to be caused by protein crowding. In addition, there is no evidence of a mechanism that confines proteins at a sufficient concentration to generate steric hindrance between proteins enough to drive membrane invagination. Unlike the crowding effect, our model doesn't rely on lateral confinement and restrictions of diffusion in the membrane (Derganc and Copic 2016). Furthermore, calculations of the entropic gain and pressure produced in the crowded protein layer, obtained with the Carnahan-Straling equation, assumes proteins are non-attracting (non-interacting) disks, not compatible with protein based structures.

Energy penalties for bending of the membrane | We calculated the membrane bending energy with the standard Helfrich model for the membrane profile obtained by equation (3.1) and

considered a membrane bending modulus κ_m of 12.5•K_BT (Helfrich 1973, Harmandaris and Deserno 2006, Carlsson and Bayly 2014):

$$U_{em} = 11 \sqrt{\left(\frac{\pi^3}{32}\right) \left(\frac{h_0}{R_0}\right)^2 \kappa_m};$$
(3.2)

We determined the energy required to generate a 70 nm deep invagination to be 3 x 10^{-18} J.

Energy penalties for elastic and viscous deformation of the cytosol | We assumed that the viscoelastic cytosol behaves as a Kelvin-Voigt material and that the total stress is equal to the sum of the elastic and viscous stresses, such that:

$$\sigma = \varepsilon E_i + \dot{\varepsilon}\eta;$$
(3.3)

, where η is the cytosol viscosity at a specific frequency f_x obtained with:

$$\eta = \frac{G''}{2\pi f_x};$$
(3.4)

For stringency, we used a Young's (or elastic) modulus (E) for the cytosol of 45 Pa (see Eq. 3.6 below) and calculated the deformation with the droplet radius (1.18 x 10^{-7} m) over the cell radius (2 x 10^{-6} m). We obtained an elastic stress of 3 Pa.
We next determined η at 0.5 Hz to be 0.35 Pa•s. and the deformation rate of 0.004 s^{-1}, for a droplet velocity v of 7.4 x 10^{-9} m•s^{-1} (Fig. S12).

$$\dot{\varepsilon} = \frac{v}{6\pi R_{drop}};$$
(3.5)

, which gives a negligible viscous stress of 0.0014 Pa. With a volume of 2.42 x 10^{-21} m^3, the total stress of 3.0014 Pa corresponds to an energy cost of 7.26 x 10^{-21} J to displace the viscoelastic cytosol.

Cortical droplet material properties and contact angle
We determined the values of the elastic modulus of the cytosol under the assumption that compressible biological materials have a Poisson's ratio (v), which relates all material moduli to each other, of 0.45 (or between 0.3 and 0.5) (Zhang, Soman et al. 2013). We then used the relationship between shear modulus (G) and Young's (or elastic) modulus (E):

$$E_i = 2(1 + v_i)G_i;$$
(3.6)

to calculate an approximate elastic modulus of 45 Pa for the cytosol from the G' of 15 Pa at 1 Hz. This strain rate was used to consider a G' near the elastic plateau of the material response. With the volume of displaced cytosol and this modulus value, we could determine the mechanical stress imposed on the cytosol to be ~3 Pa (see Eq. 3.3-3.5). This corresponds to a compression force (F) of ≈ 1.4 x 10^{-13} N. We then isolated the equivalent modulus (E') from Hertz elastic contact equation

$$F = \frac{4}{3} E'_{ij} R'_{ij}^{\frac{1}{2}} \delta_{ij}^{\frac{3}{2}};$$

(3.7)

into

$$E'_{ij} = \frac{4F}{3 R'_{ij}^{\frac{1}{2}} \delta_{ij}^{\frac{3}{2}}};$$

(3.8)

, where δ_{ij} is the interface indentation (or invagination depth), to estimate the respective elastic moduli of the cytosol and the droplet, again under the assumption that both materials have a Poisson's ratio of 0.45. The equivalent modulus is determined by:

$$\frac{1}{E'_{ij}} = \frac{(1 + v_i)^2}{E_i} + \frac{\left(1 + v_j\right)^2}{E_j};$$

(3.9)

where E_i and E_j are the respective elastic moduli of the objects in contact and

$$\frac{1}{R'_{ij}} = \frac{1}{R_i} + \frac{1}{R_j};$$

(3.10)

for contact between two spheres of radii R_i and R_j. These relationships gave us a cortical droplet elastic modulus of 59 Pa.

Assuming that gravity is negligible, the droplet can be treated as a sectional arc of a sphere or hemispherical cap alone (Fig. S4b) and we can estimate the droplet contact angle;

$$\theta = 2 \cdot \tan^{-1}\left(\frac{h}{d}\right)$$

(3.11)

, where d is droplet radius and h is droplet height. Based on our 2D dSTORM measures we obtained a contact angle of about 97°. Note that at the hundred nanometer scale, droplet wetting geometries are also affected by evaporation and line tension at the three-phase contact line.

Theoretical model based on elastic and adhesive contact mechanics

To explain how phase separation of disordered proteins into a 100 nm-scale viscoelastic body can invaginate the membrane (in the absence of turgor, F-actin polymerization and steric effects), we propose a model in which elastic and adhesive contact mechanics can generate enough energy (estimated from membrane bending to be ≈3 x 10^{-18} J) to drive local invagination of the membrane.

We explored the idea that when cortical droplets are nucleated between the membrane and cytoplasm, new interfaces are created and the free energy available on the droplet interfaces can produce work to deform both surrounding substrates (membrane and cytosol). We thus assume that free energy is released upon phase separation and adhesion of the cortical droplet to neighbor structures, which is converted into mechanical work.

Calculations and graphics of the elastic, viscous, surface and adhesive energies in our model were performed in either Maple or the R software environment. The parameters, variables and relationships we used in the calculation are listed in Tables S1 and S2. A summary of the invagination and energy results we obtained with these specific parameters are in Table S3. We describe below the details of the model.

General mechanic model to bend the membrane | We first propose a general model where the energy penalties to create interfaces around the droplet and deform the cytosol and the membrane follow a super-linear growth as a function of invagination depths δ (of both cytosol and membrane), whereas the free energy released by droplet phase separation is linear. We expressed the relationship between these two general energy terms and the total energy U with the power-law function:

$$U \sim \phi \cdot \delta^{1+\varepsilon} - \psi \cdot \delta; \tag{4.1}$$

, where ϕ is the energy penalty term, ψ is the available work and the exponent $\varepsilon > 0$. When δ is isolated from the partial derivative of equation (4.0), such as:

$$\frac{\partial U}{\partial \delta} = \phi(1 + \varepsilon) \cdot \delta^{\varepsilon} - \psi;$$

$$\delta^* = \left(\frac{\psi}{\phi \, (1 + \varepsilon)} \right)^{\frac{1}{\varepsilon}}; \tag{4.2}$$

15

, we observe that our model predicts that δ scales with ϕ and ψ:

$$\delta^* \sim \frac{\psi}{\phi};$$ (4.3)

We provide below a proof for this model, where ϕ is decomposed into individual elastic, viscous friction and surface stress terms and ψ is fragmented in the work of adhesion from the respective droplets interfaces. We also describe the quantities contained within these individual terms; either directly measured, calculated or estimated.

Interfaces at equilibrium on cortical droplets | Parallel to the membrane plane, surface energies formed by the droplet (d), cytosol (c) and membrane (m) come to equilibrium as described by Young's equation:

$$\gamma_{cm} = \gamma_{dm} + \gamma_{dc} \cdot \cos\theta;$$ (4.4)

With a contact angle of about 97°, the cytosol-membrane surface tension (γ_{cm}) is predicted to be approximately equal to the droplet-membrane surface tension (γ_{dm}). We determined the values of γ_{dc} and γ_{dm} next.

Surface tension at cortical droplet interfaces | We assumed an apparent Young's modulus (E_{cell}) of 1 kPa, determined from atomic force microscopy on haploid yeast spheroblast (Munder, Midtvedt et al. 2016). We assumed that this modulus represents the bulk material properties of both membrane and cytosol when deformed towards the cell interior, as for a CME-driven invagination. We then calculated the overall mechanical stress in the system with Hooke's law:

$$\sigma = \varepsilon E_i;$$ (4.5)

to create the U-shape membrane geometry observed by EM. The deformation ε of the membrane was decomposed to represent stretching of an elastic band, where deformation equals length difference over original length. For our U-shaped deformation the linear contour was established at 174.2 nm, whereas the same membrane line measured $\approx$ 80 nm before invagination. This gives us a deformation of 1.18 (dimensionless) and a stress of 1178 Pa.

This mechanical stress corresponds to the pressure difference ΔP experienced by the cytoplasm and the membrane due to the presence of the cortical droplet. This pressure difference arises from adhesive, hydrostatic and elastic stress energies. We then used the Young-Laplace equation:

$$\Delta P = 2\gamma_{dc} \cdot H;$$ (4.6)

16

, where H is the mean curvature of the interface and is equal to $1/R_d$, to calculate γ_{dc} at the cytosol interface under the assumption that the droplet is circular in shape. Equation (4.6) determines the pressure difference across the droplet-cytosol curved interface as a function of surface energy, and gives a droplet/cytosol interfacial tension γ_{dc} of 7×10^{-5} N•m^{-1}.

Based on Young's equation (4.4) and the cortical droplet-membrane contact angle θ value, the relationships between interfacial tensions is:

$$\gamma_{cm} = \gamma_{dm} + \gamma_{dc} \cdot \cos\theta$$
$$\gamma_{cm} = \gamma_{dm} - (8 \cdot 10^{-6}); \qquad (4.7)$$

and

$$\gamma_{dc} > \gamma_{dm}; \qquad (4.8)$$

where the droplet-membrane surface tension γ_{dm} can range between about 1.8 to 7×10^{-5} N•m^{-1}. The γ_{dm} limits also arise from equation (4.9) below.

Biopolymeric constraints on interfacial tension values | The interfacial tension γ of a fluid droplet is inversely proportional to the square of the length ξ of its discrete elements (i.e. the individual biopolymers), we used this relationship to estimate maximal and minimal γ values:

$$\gamma = \frac{k_B T}{\xi^2}; \qquad (4.9)$$

, where k_B is the Boltzmann constant and T is temperature in kelvin (Brangwynne, Mitchison et al. 2011). The interfacial tension values for protein based biological droplets (in which protein radii range from 1 to 10 nm) should be on the order of 1×10^{-5} N•m^{-1} to 1×10^{-4} N•m^{-1}.

Work of adhesion at cortical droplet interfaces | To directly estimate the work of adhesion at the cortical droplet interfaces, we used the Young-Dupré equation:

$$W_{dm} = \gamma_{dc} \cdot (1 + \cos\theta); \qquad (4.10)$$

that implies a direct relationship between work of adhesion of an interface (W_{ij}), the droplet contact angle and the surface tension γ_{dc}. We could determine the work of adhesion at the membrane interface W_{dm} to be 6×10^{-5} N•m^{-1}.

We also combined the Young's equation (4.1) and the Dupré relationship:

$$W_{dc} = \gamma_{dm} + \gamma_{cm} - \gamma_{dc}; \qquad (4.11)$$

17

to express the work of adhesion at the cortical droplet-cytosol interface W_{dc}:

$$W_{dc} = 2\gamma_{dm} + \gamma_{dc} \cdot (\cos\theta - 1); \qquad (4.12)$$

in terms of interfacial tension at cortical droplet interfaces with both membrane and cytosol. We could thus estimate the maximal W_{dc} value to be 6×10^{-5} N•m^{-1}, under the assumption that $\gamma_{dm} \approx \gamma_{dc}$.

Young-Dupré regime dominates nanoscopic viscoelastic bodies | We determined in parallel whether adhesion dominates the mechanical potential of cortical droplets, as opposed to capillary effects. Under so called elasto-capillary action, droplet interfacial tension (ϒ) can deform an elastic sheet as a function of either droplet radius (R) or the thickness (h) and elastic modulus (E) of the slender material in contact with the droplet; in our case, the plasma membrane (Roman and Bico 2010). We can assume that the phospholipid bilayer membrane is about 10 nm thick and the cell has a bulk elastic modulus E of 1 kPa (Munder, Midtvedt et al. 2016). With a surface tension γ_{dc} of 7×10^{-5} N•m^{-1}, we determined that R is larger and h is about equal to the elasto-capillary length:

$$\frac{\Upsilon}{E} \, ; \qquad (4.13)$$

, and the membrane sheet should remain undeformed at the 3-line contact point by interfacial tension alone (Fig. 4a). This prediction is also consistent with EM data where the membrane doesn't bulge out under the Laplace pressure within droplets on cortical sites (Idrissi, Grotsch et al. 2008). In this scenario our system should obey the Young-Dupré equation and deformation can only come from work of adhesion.

Elastic-adhesive model to deform membrane and cytosol under action of cortical droplet phase separation | Johnson-Kendall-Roberts (JKR) theory describes how non-flat surfaces stick together and conform to one another to minimize their interfacial energy. When they adhere to one another, soft and compliant materials such as the membrane and cytoplasm are subject to a deformation limited by elastic strain. Style, *et al.* adapted the JKR theory of contact mechanics to describe the contact surface geometry between a microscopic rigid particle and a soft substrate (Style, Hyland et al. 2013); we followed a similar approach to estimate model 4.1 parameters and test our hypothesis.

If we consider the two droplet interfaces where deformation occurs, both membrane and cytoplasm, the energy penalty to create these curved surfaces (or interfaces) are equal to the sum of elastic, viscous and surface energies.

To build a complete energy model, the elastic energy penalties were determined with the JKR theory. Since the geometry of the contact surface corresponds to the cortical droplet geometry itself, we calculated the elastic penalties $U_{e|y}$ to deform both interfaces as a function of invagination depth δ_{ij}:

$$U_{e|y}\left(\delta_{ij}, E'_{ij}, R'_{ij}\right) = c E'_{ij} R'^{\frac{1}{2}}_{ij} \cdot \delta_{ij}^{\frac{5}{2}};$$ (4.14)

where E'$_{ij}$ and R'$_{ij}$ are calculated with (3.5) and (3.6) respectively and c is a constant.

$$c = \frac{8}{15} \cdot \sqrt{3};$$ (4.15)

We incorporated a correction for the membrane elastic penalty to compensate for the reduced JKR accuracy at the hundred nanometer scale and for soft materials (Style, Hyland et al. 2013) by addition of the Helfrich Hamiltonian of membrane bending at individual δ_{ij} values. We substituted h_0 in equation (3.2.0) for δ_{ij} and assumed a fixed radius of invagination R_{ij} to get the relationship:

$$U_{em.corr}\left(\delta_{ij}\right) = 11 \sqrt{\left(\frac{\pi^3}{32}\right)} \left(\frac{\delta_{ij}}{R_{ij}}\right)^2 \kappa_m;$$ (4.16)

We calculated a corrected energy cost of $\approx 1 \times 10^{-18}$ J to deform the membrane (Table S3). The cytoplasm elastic energy barrier did not require correction and we assumed no elastic nor viscous droplet deformation in our model.

JKR theory is also less accurate for very soft materials and small particles because the model neglects surface stresses (Style, Hyland et al. 2013). Inclusion of energy penalties to increase surface length at the interfaces was proposed by Style *et al.* to compensate for this reduced accuracy (Style, Hyland et al. 2013). We incorporated the surface penalties ($U_{i|y}$) for the formation of the new interfaces into our model with the function;

$$U_{i|y}\left(\delta_{ij}, \gamma_{ij}\right) = \pi \gamma_{ij} \cdot \delta_{ij}^2$$ (4.17)

, where the respective interfacial tensions γ_{dc} and γ_{dm} determine the energy cost to increase the interfacial areas. The energy to form the droplet/cytosol interface is $\approx 1 \times 10^{-18}$ J and is equivalent to the combined elastic penalties. These energy values confirm that at the hundreds of nanometers scale, surface stress can dominate (or equate) elasticity in material responses to

deformation. With this approach, we propose a more comprehensive model of the energy required to deform the membrane on cortical sites, that also takes into account creation of new surfaces and deformation of the cytosol.

We also incorporated an additional energy penalties $U_{v|y}$ to displace the viscous cytosol with the equation:

$$U_{v|y}\left(\delta_{ij}, R'_{ij}, \eta, \dot{x}\right) = \eta \dot{x} \delta_{ij} \cdot 6\pi R'_{ij}; \tag{4.18}$$

, where the displacement rate is the droplet maximum velocity of 7.4×10^{-9} m•s^{-1} (Fig. S12).

If the conversion of the energy released by adhesive contact into mechanical energy is above the total energy barrier, the droplet should drive membrane invagination. The extent of membrane invagination will be limited by the free energy available. For the purpose of our model, we calculated the energy of adhesion ($U_{a|y}$) with the JKR term:

$$U_{a|y}\left(\delta_{ij}, W_{ij}, R'_{ij}\right) = W_{ij} R'_{ij} \cdot \delta_{ij} ; \tag{4.19}$$

where W_{ij} is the work of adhesion at each interface, as determined by equations (4.10) and (4.12), respectively. The work of adhesion refers to the energy released in the wetting process of the cortical droplet on the membrane, it equals the work needed to separate the two adjacent phases and is given by the Dupré equation (4.11).

We then integrated the elastic (4.14, 4.16), interfacial (4.17), viscous (4.18) and adhesion (4.19) terms into a complete energy equation for i,j interfaces, where:

$$\begin{aligned} i &= \{droplet\}; \\ j &= \{membrane, cortex\}; \end{aligned} \tag{4.20}$$

into

$$U_{total}\left(\delta_{dm}, \delta_{dc}, \gamma_{dm}, \gamma_{dc}, W_{dm}, W_{dc}\right) =$$

$$cE'_{dm}R'_{dm}{}^{\frac{1}{2}} \cdot \delta_{dm}{}^{\frac{5}{2}} + 11\sqrt{\left(\frac{\pi^3}{32}\right)}\left(\frac{\delta_{dm}}{R_{dm}}\right)^2 \kappa_m + \pi\gamma_{dm} \cdot \delta_{dm}{}^2 - W_{dm}R'_{dm} \cdot \delta_{dm}$$

$$+cE'_{dc}R'_{dc}{}^{\frac{1}{2}} \cdot \delta_{dc}{}^{\frac{5}{2}} + \pi\gamma_{dc} \cdot \delta_{dc}{}^2 + \eta\dot{x}6\pi R'_{dc} \cdot \delta_{dc} - W_{dc}R'_{dc} \cdot \delta_{dc}; \tag{4.21}$$

To reduce the number of free fitting parameters, we first defined the values of the variables that were measured (or calculated) and expressed the work of adhesion of each interface W_{ij}, as determined by (4.10) and (4.12) respectively:

$$U_{total}(\delta_{dm}, \delta_{dc}, \gamma_{dm}) =$$

$$cE'_{dm}R'_{dm}{}^{\frac{1}{2}} \cdot \delta_{dm}{}^{\frac{5}{2}} + 11\sqrt{\left(\frac{\pi^3}{32}\right)\left(\frac{\delta_{dm}}{R_{dm}}\right)^2 \kappa_m} + \pi\gamma_{dm} \cdot \delta_{dm}{}^2 - \frac{7\pi R'_{dm}\gamma_{dc} \cdot \delta_{dm}}{4}$$

$$+ cE'_{dc}R'_{dc}{}^{\frac{1}{2}} \cdot \delta_{dc}{}^{\frac{5}{2}} + \pi\gamma_{dc} \cdot \delta_{dc}{}^2 + \eta\dot{x}6\pi R'_{dc} \cdot \delta_{dc}$$

$$- \left(4\pi R'_{dc}\gamma_{dm} - \frac{9\pi R'_{dc}\gamma_{dc}}{4}\right) \cdot \delta_{dc} \; ; \qquad (4.22)$$

Finally, we coupled the membrane and cytosol invagination or penetration depth δ_{ij} with a simple function:

$$\delta_{dc} \to f(\delta_{dm}) = \mu \cdot \delta_{dm} + k; \qquad (4.23)$$

, that reflects a mechanical coupling assumption, where μ and k are constants that were solved for the $(\delta_{dm}, \delta_{dc})$ coordinates $(0,0)$ and $(7 \times 10^{-8}, 1.2 \times 10^{-7})$ to 1.7 and 0 respectively. This linear relationship between δ_{dm} and δ_{dc} ensures that a critical droplet volume is conserved and that invagination values are consistent with the distribution of droplet size and membrane invagination from imaging and EM data (Idrissi, Blasco et al. 2012). This single δ_{ij} variable was henceforth referred to as δ (without any index).

We ended with a total energy function with 2 independent variables:

$$U_{total}(\delta, \gamma_{dm}) = cE'_{dm}R'_{dm}{}^{\frac{1}{2}} \cdot \delta^{\frac{5}{2}} + 11\sqrt{\left(\frac{\pi^3}{32}\right)\left(\frac{\delta}{R_{dm}}\right)^2 \kappa_m} + \pi\gamma_{dm} \cdot \delta^2 - \frac{7\pi R'_{dm}\gamma_{dc} \cdot \delta}{4}$$

$$+ cE'_{dc}R'_{dc}{}^{\frac{1}{2}} \cdot (\mu\delta)^{\frac{5}{2}} + \pi\gamma_{dc} \cdot (\mu\delta)^2 + \eta\dot{x}6\pi R'_{dc} \cdot (\mu\delta)$$

$$- \left(4\pi R'_{dc}\gamma_{dm} - \frac{9\pi R'_{dc}\gamma_{dc}}{4}\right) \cdot (\mu\delta); \qquad (4.24)$$

that expresses the total energy as a function of membrane invagination and interfacial tension of the cortical droplet-membrane interface.

We explicitly defined the mechanical strain term of the model (4.1):

$$\phi \cdot \delta^{1+\varepsilon} = \left(\begin{array}{c} cE'_{dm}R'_{dm}{}^{\frac{1}{2}} + 11\sqrt{\left(\frac{\pi^3}{32}\right)\left(\frac{\delta^{-\frac{1}{2}}}{R_{dm}{}^2}\right) \kappa_m} + \pi\gamma_{dm} \cdot \delta^{-\frac{1}{2}} + cE'_{dc}R'_{dc}{}^{\frac{1}{2}}\mu^{\frac{5}{2}} \\[2mm] + \pi\gamma_{dc} \cdot (\mu\delta)^{-\frac{1}{2}} + \eta\dot{x}6\pi R'_{dc} \cdot (\mu\delta)^{-\frac{3}{2}} \end{array} \right) \cdot \delta^{\frac{5}{2}}; \quad (4.25)$$

, where the power law variable ε of 1.5 reflects the energy penalties for parabolic shaped cytosol and membrane deformations, and the mechanical work term of (4.1):

$$\psi \cdot \delta = \left(\frac{7\pi R'_{dm}\gamma_{dc}}{4} + \mu \left(4\pi R'_{dc}\gamma_{dm} - \frac{9\pi R'_{dc}\gamma_{dc}}{4} \right) \right) \cdot \delta; \qquad (4.26)$$

We minimized the function (4.24) on the δ_{dm} (1 x 10^{-9} m to 7 x 10^{-9} m) and γ_{dm} interval (1.8 x 10^{-5} N•m^{-1} to 7 x 10^{-5} N•m^{-1}) and obtained an energy minimum. This corresponds to an energy optimal invagination of 41 nm with a maximal γ_{dm} of 7 x 10^{-5} N•m^{-1}. For the γ_{dm} value of membrane invagination is favorable up to a depth of 80 nm (Fig. S15). We also determined that to achieve an energy favorable membrane invagination of 70 nm (total energy U_{total} equal or less than 0 J) the system requires a minimal γ_{dm} of 6 x 10^{-5} N•m^{-1} (Fig. S15d). With this lower γ_{dm} value, the system would reach a minimum energy with a membrane invagination of 35 nm (Fig. S15e).

With the geometric data and estimates of γ_{dc}, we determined the energy required to create new interfaces U_i around the droplet and the adhesive energy U_a at these interfaces (Fig. 4b, Fig. S15, Supplementary method; Eq. 4.17,4.19). At a δ value of 41 nm (corresponds to energy minimum), we summed the energy penalties (ϕ term) and estimated a total energy barrier of 2.4 × 10^{-18} J to deform the membrane and cytosol in contact with the cortical droplet. This energy cost includes the elastic, viscous, and interfacial stress penalties (Fig. 4b, Supplementary method; Eq. 4.25, Table S4). The interfacial stress penalty to form the droplet/cytosol interface is 1.0 × 10^{-18} J and is equivalent to the membrane elastic penalties. These results are consistent with studies of artificial materials where at the 100 nm scale, surface stress can dominate elasticity in material responses to deformation (Style, Hyland et al. 2013). When we consider the energy favourable domain, our model correctly predicts the magnitude of invagination (about 40 nm to 80 nm) that is accessible for a successful invagination that leads to vesicle excision (Fig. S15e).

Calculation of adhesive energy on the droplet interfaces | To relate the free energy on the cortical droplet interface to density of molecular interaction on the droplet surface, we divided the adhesion energy of 3 x 10^{-18} J at the cytosol interface by the protein density on the droplet surface. We estimated, based on our dextran exclusion experiment, that proteins on the droplet surface are arranged in a matrix with mesh size of 10 nm (or less). If we assume an average protein filament width of 2 nm, for a droplet area of 6.93 x 10^{-14} m^2, we obtain a minimum of 1.4 x 10^3 protein segments on the droplet surface, based on the assumption that single proteins maximize their interactions with the cytosol elements, which is not likely given that these proteins phase separate from the bulk and favour intermolecular interactions. To maximize the adhesive energy per protein exposed on the interface, we determined the minimum amount of protein that the droplet could be composed of to be about 2 x 10^{-21} moles on its surface and a

maximal adhesive energy density of 1.3 kJ•mol^{-1}. Conversely, this approach gives a maximum of 2.8 x 10^{10} molecules on the surface, or 4.7 x 10^{-14} moles of proteins, and a minimal adhesive energy of 6.3 x 10^{-5} J•mol^{-1}. To be stringent, we considered the former.

Supplementary Figures:
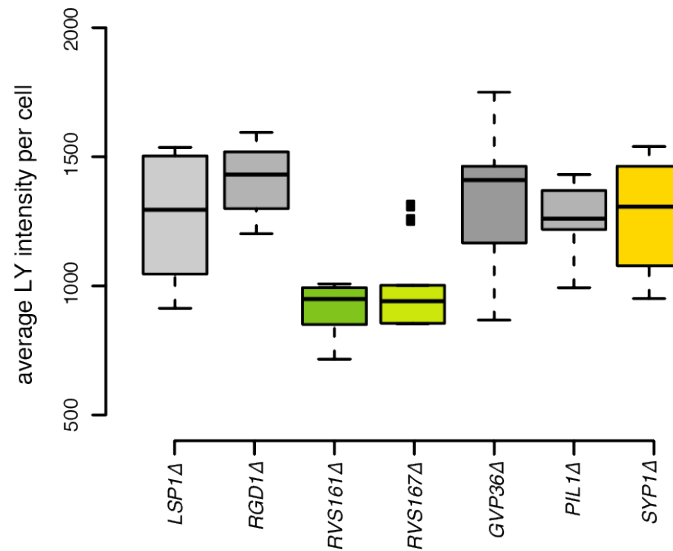
Figure S1 | Syp1 protein is the only BAR domain protein recruited to CME nucleation sites prior to F-actin polymerization and is not required for CME. F-BAR protein Syp1-mCherry and N-BAR proteins Rvs161-mCherry and Rvs167-mCherry (scission phase) were colocalized with both Sla1-GFP (early phase marker) and Sac6-GFP (late actin phase marker). Line scan analyses on 2-channel images were performed across the Sla1-GFP or Sac6-GFP puncta and plotted on 8-bit intensity range. LY uptake was assessed for each strain by fluorescence intensity (n = 100 cells).
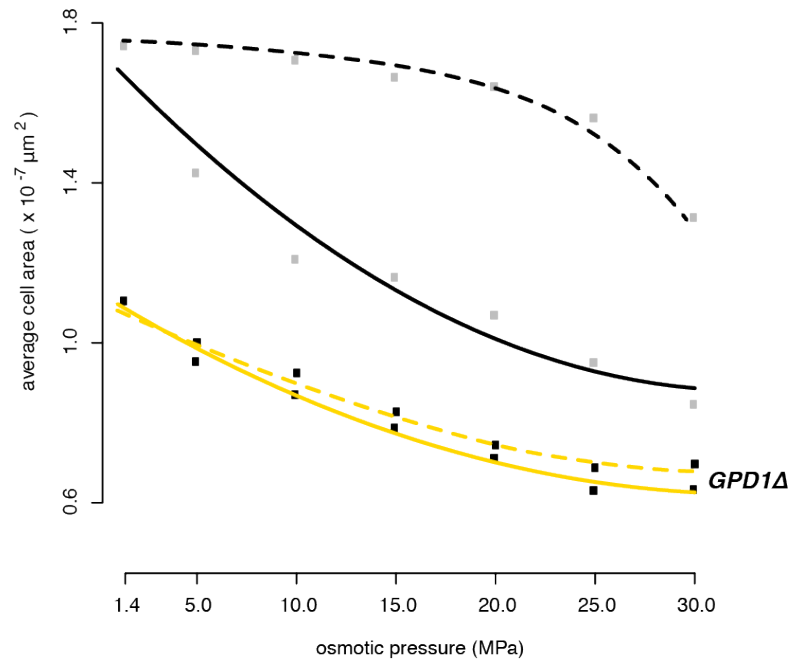
Figure S2 | *GPD1Δ* cells cannot maintain turgor. To detect turgor pressure and cell size adaptation to osmotic shock in wild type (black) and *GPD1Δ* strain (yellow), we monitored by fluorescent microscopy the cross-sectional area (μm^2) of shocked cells (solid lines) and adapted cells (dashed lines) in water-glycerol binary solutions from 1.4 MPa to 30 MPa. Points represent mean area values (n=200 cells).
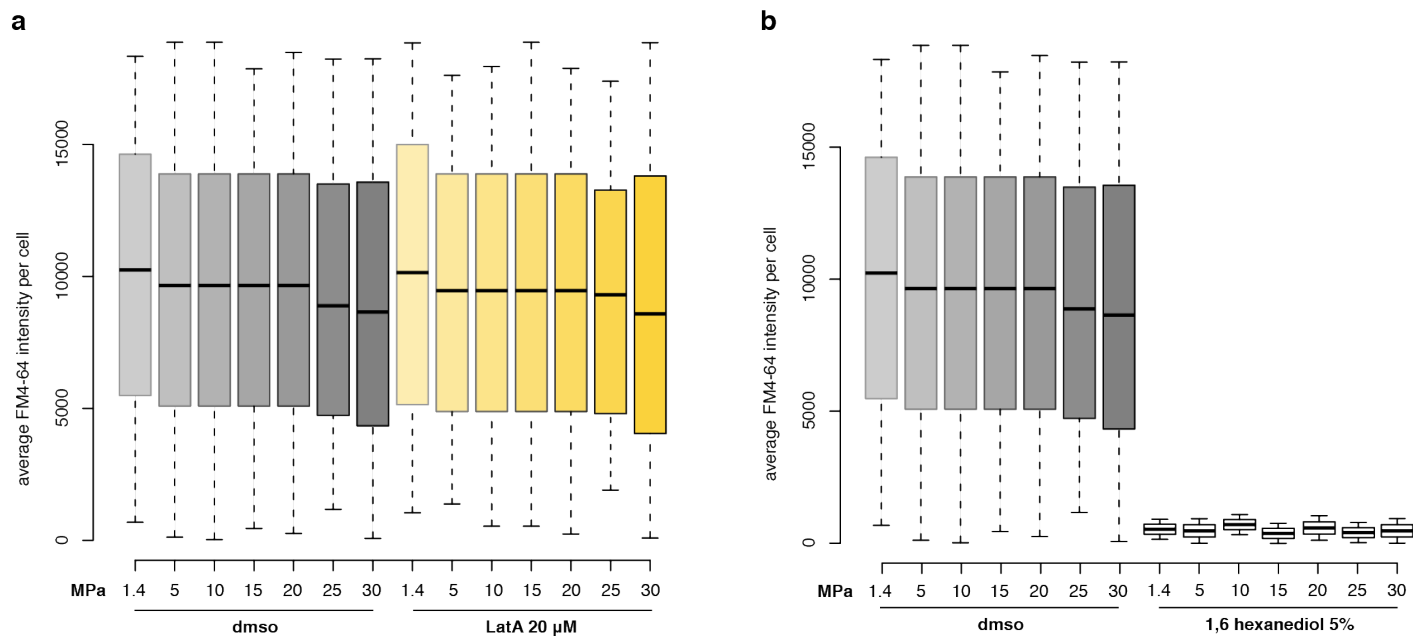
Figure S3 | Membrane-associated FM4-64 fluorescent probe uptake was quantitatively assessed by fluorescence imaging. (a) *GPD1Δ* strains undergo normal CME in the absence of actin polymerization (Latrunclulin A-treated), (b) but not when treated with 1,6-hexanediol, n = 900 cells for each condition.
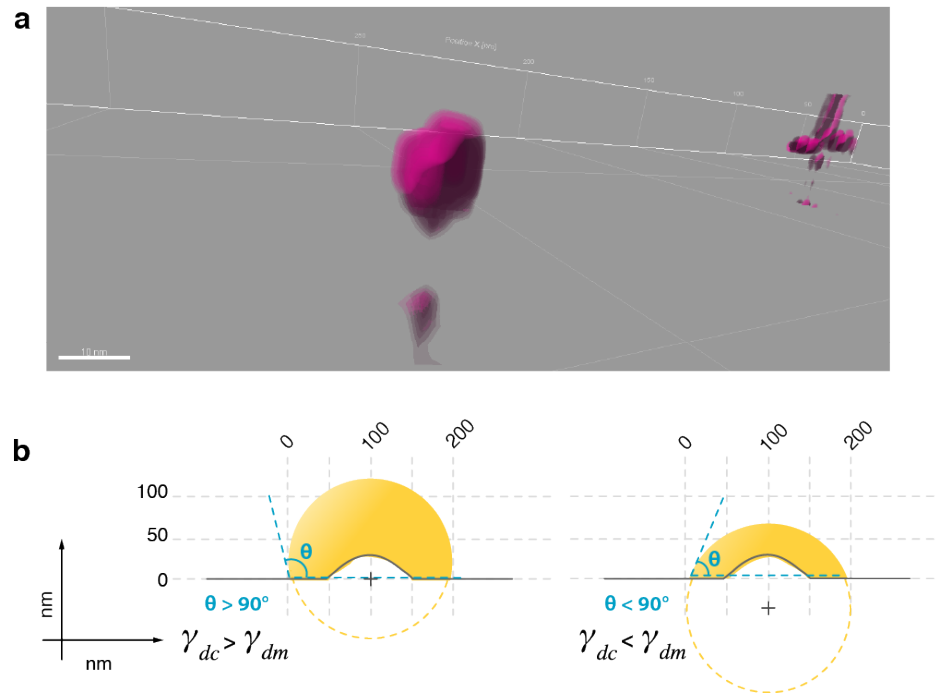
Figure S4 | Geometry of coat protein distribution at cortical sites with super-resolution (dSTORM) fluorescence imaging of Alexa647-labeled Sla1-GFP. Reconstructed images for these proteins show circular structures when viewed from top but are narrow ellipses when imaged at the equator of cells. (a) 3D dSTORM acquisition was achieved with an astigmatic lens. We gated single fluorophore emission events with a 16-bit intensity above 250. z location was determined based on a calibration curve made with TetraSpeck beads (Supplementary methods). We exported the (x,y,z) coordinates from Wave Tracer to Imaris Software to build 3D reconstructions of droplets, consistent with hemispherical domes, as suggested by the asymmetrical 2D projections (Fig 2a). (b) Cortical droplet width (209 ± 10nm) and height (118 ± 6nm) give a contact angle (θ) of $\sim 97°$. θ above $90°$ is indicative of poor wettability whereas a θ below $90°$ would wet the membrane. θ also informs on the relationships between the surface tensions (γ_x) at the interfaces.
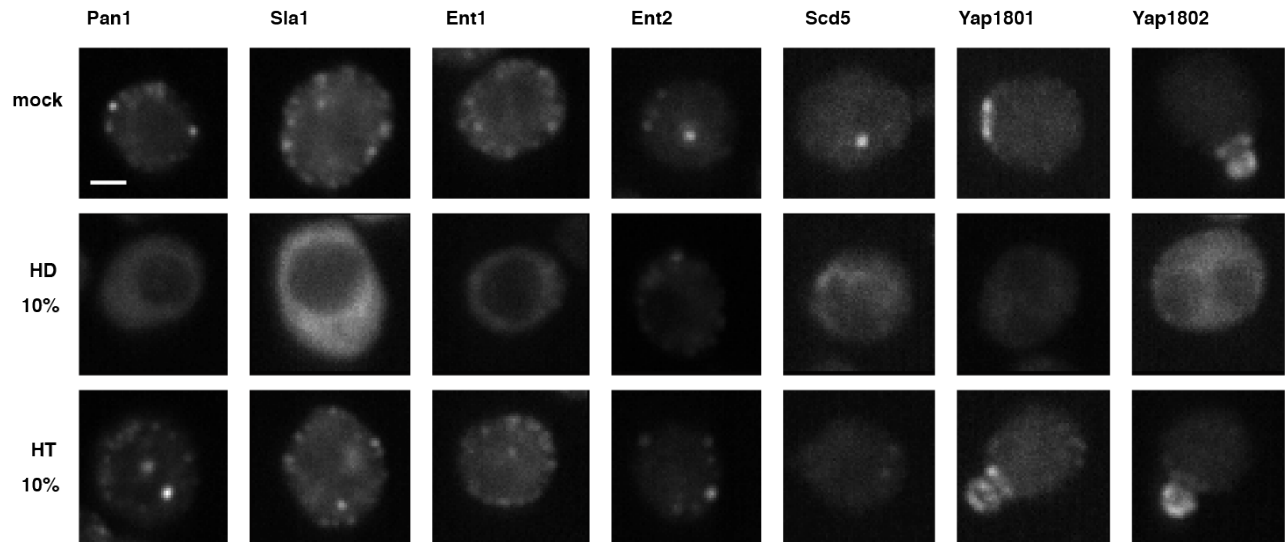
Figure S5 | Cortical patch-associated PLD-containing proteins fail to form puncta in cells treated with 1,6-hexanediol (HD), but behave normally upon 1,2,3-hexanetriol (HT) treatment. Fluorescence images of GFP-tagged Pan1, Sla1, Sla2, Ent1, Ent2, Scd5, Yap1801 and Yap1082 puncta 5 min after treatment with either DMSO, 1,6-hexanediol or 1,2,3-hexanetriol, images where acquired with InCell6000 confocal microscope. Scale bar 2 μm.
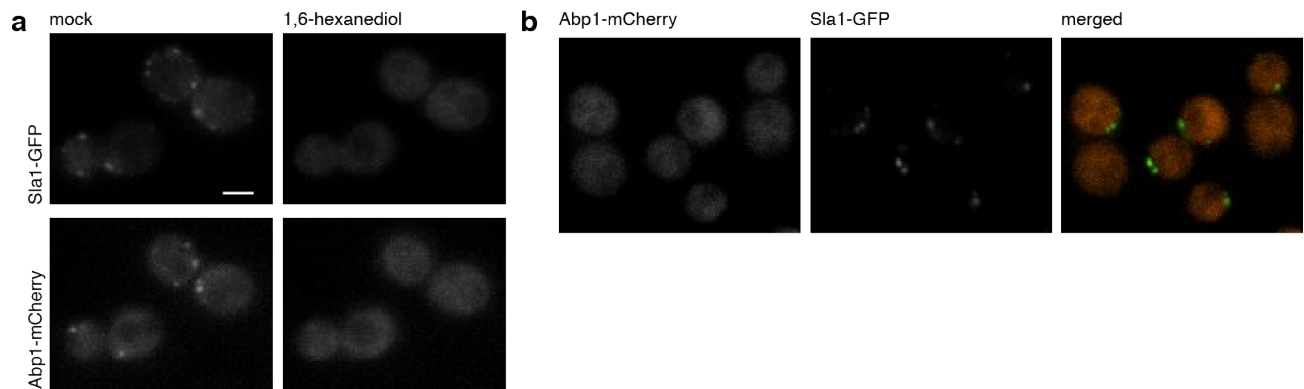

Figure S6 | (a) Pulse-chase experiments with HD show that HD-dependent dissolution of Sla1 puncta is reversible. Images from fluorescent monitoring through time of Sla1-GFP and Abp1-mCherry under a pulse-chase cycle of 10% HD. Low Fluorescence Medium (LFM) was replaced with 10% HD LFM at 10 min and replaced with fresh LFM at 15 min. Maximal intensity projections of Z-stacks are shown before HD treatment (left), 2.5 min incubation with HD (middle) and 3.5 min after HD removal (right). Scale bar 2 μm. See also Supplementary movie 1. (b) F-actin polymerization is also disrupted by Latrunculin A. Assessment of Abp1-mCherry actin structures by fluorescence microscopy in presence of 5-20 μM LatA for 5 min. Maximal intensity projections of Z-stacks of cells before (left) and after (right) treatment are shown. Scale bar 2 μm.
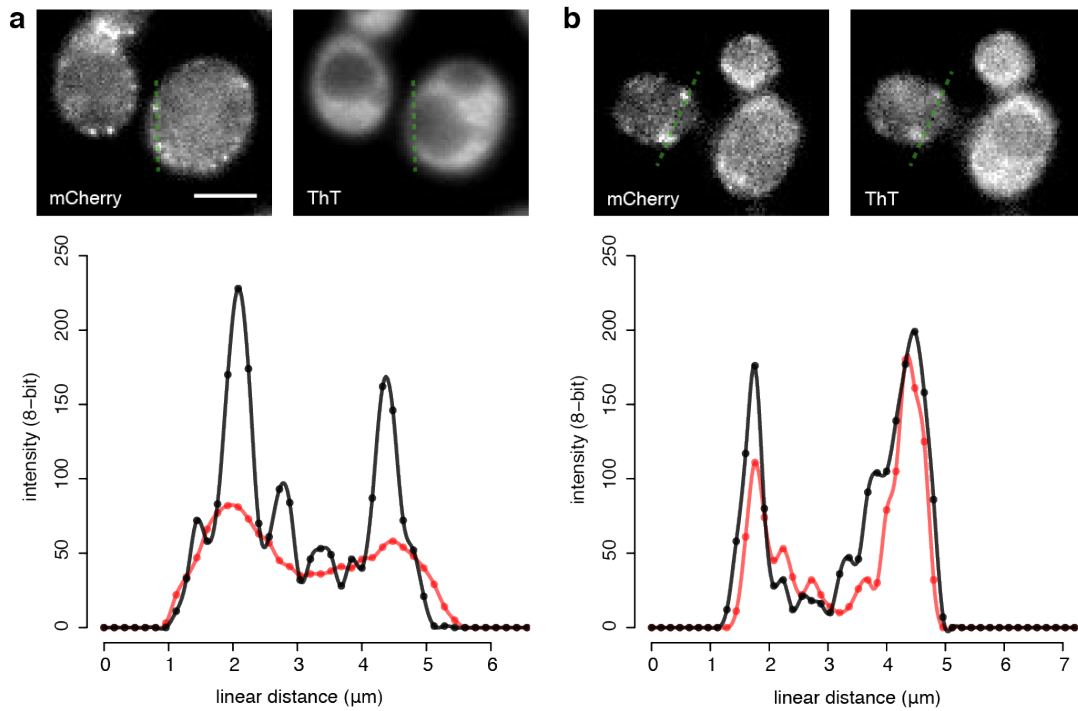
Figure S7 | We observed no colocalization of Thioflavin T (ThT) with Sla1-mCherry puncta. (a) Fluorescence microscopy of Sla1-mCherry (upper left), ThT stain (upper right) and line scan analysis (lower panel) for the dashed line in green. Scale bar, 2 μm (b) Fluorescence microscopy of Sup35-mCherry (upper left), ThT stain (upper right) and line scan analysis (lower panel) for the dashed line in green. Scale bar, 2 μm.
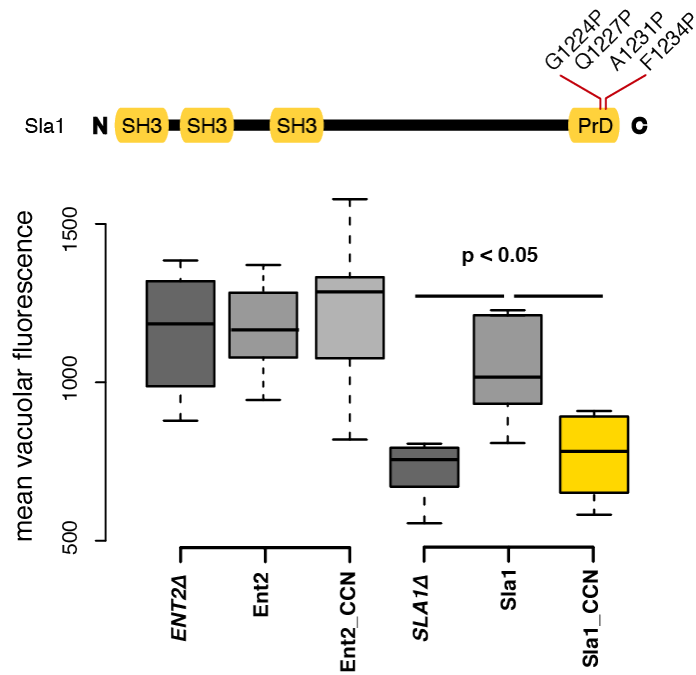
Figure S8 | Mutations of PLDs that prevent phase separation of proteins also disrupt CME. Proline mutations were introduced near or within the C-terminal PLD domains of Sla1 and Ent2 mutant strains and CME measured by fluorescence of lucifer yellow dye uptake. Positions of the mutation are shown on the schematic representation of the proteins. Introduction of such mutations into the PLDs of Ent1 and Sla1 resulted in equivalent effects of complete PLD deletion on CME-mediated lucifer yellow dye uptake. Boxplots with n > 100 cells and a t-test used to determine *P*-values.
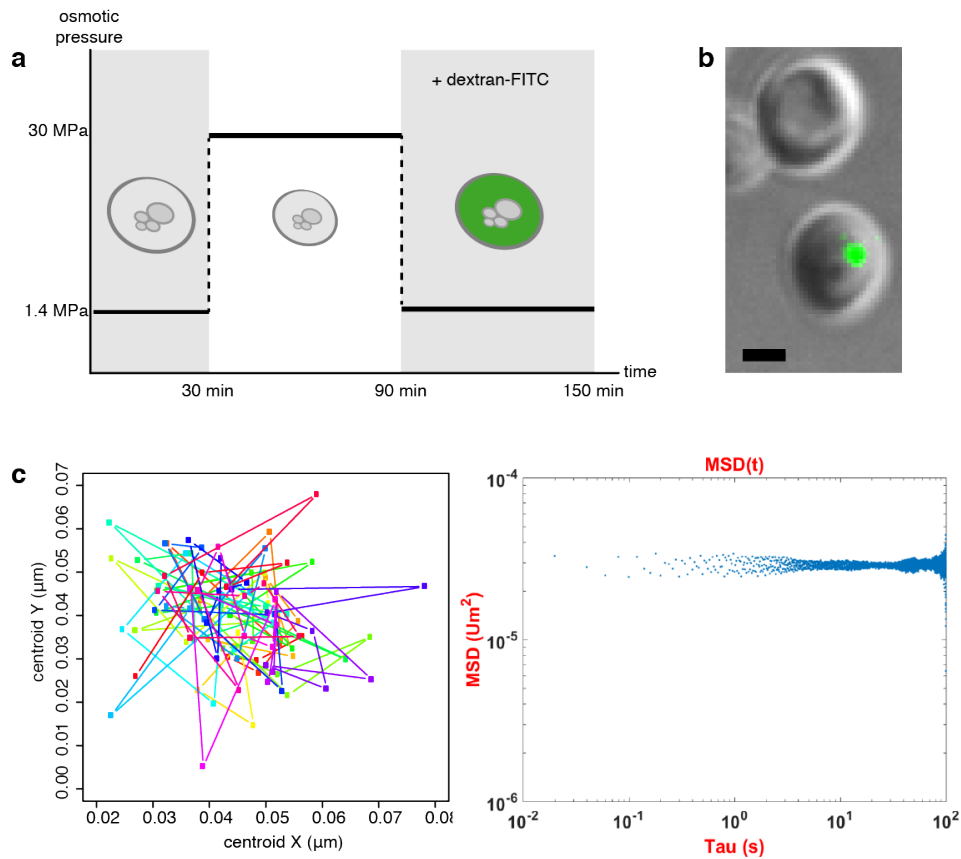
Figure S9 | Osmoporation of polystyrene beads and micro-rheology. (a) Schematic representation of the two-cycle osmotic shock used to osmoporate 200 nm polystyrene beads into haploid yeast cells. The osmoporation treatment induces a senescent-like state in most cells, but we could rescue a small fraction of cells that continue to divide in rich YPD medium. (b) Images of Sla2-Dronpa3 (green foci) cells with osmoporated beads (left panel). Scale bar is 2 μm. (c) Passive 2D displacement in x and y of 200 nm polystyrene beads measured based on centroid tracking. We observed the movement of beads by centroid tracking (middle panel) and also determined the mean square displacement (right panel). The polystyrene beads we incorporated into cells were confined within the cytosol with a MSD close to that of technical noise.
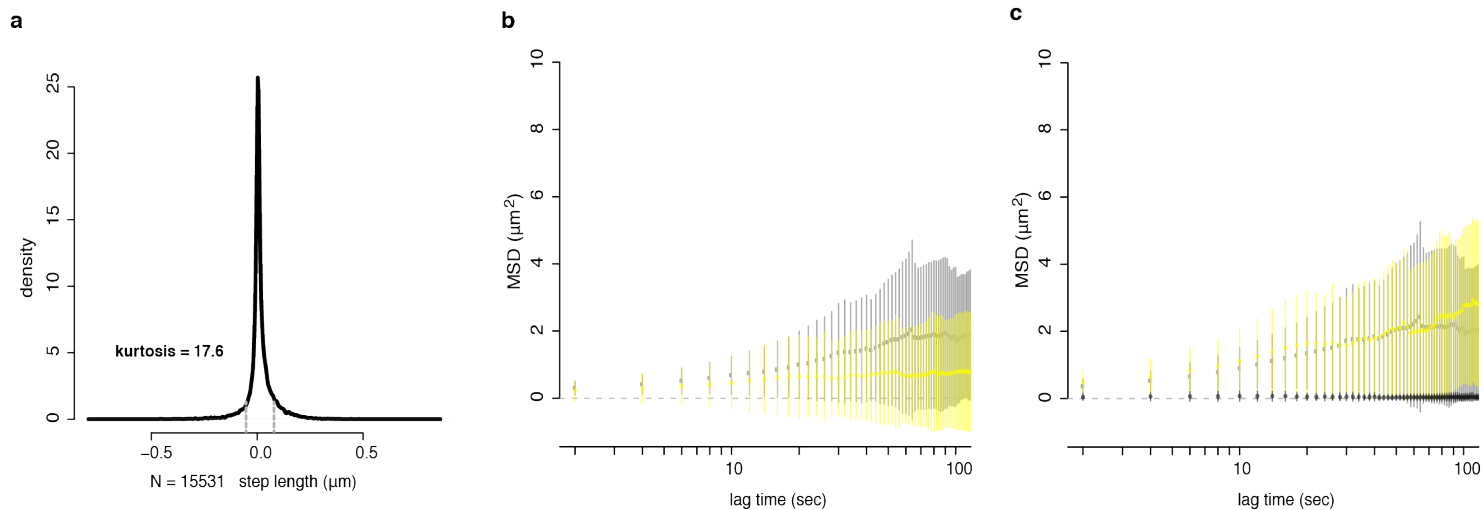
Figure S10 | We measured displacement of expressed viral capsid microNS particles labeled with GFP in both untreated and osmoporated cells. (a) Distribution of step length of expressed microNS-GFP particles determined by centroid tracking in untreated cells. (b-c) MSD of microNS particles in untreated (grey) and osmoporated (yellow) cells as a function of lag time (seconds). Data points represent mean ± standard deviation of 300 traces in untreated *versus* osmoporated cells, panel b shows raw data and panel c shows data filtered for caged particles with MSD < 1 represented in black.
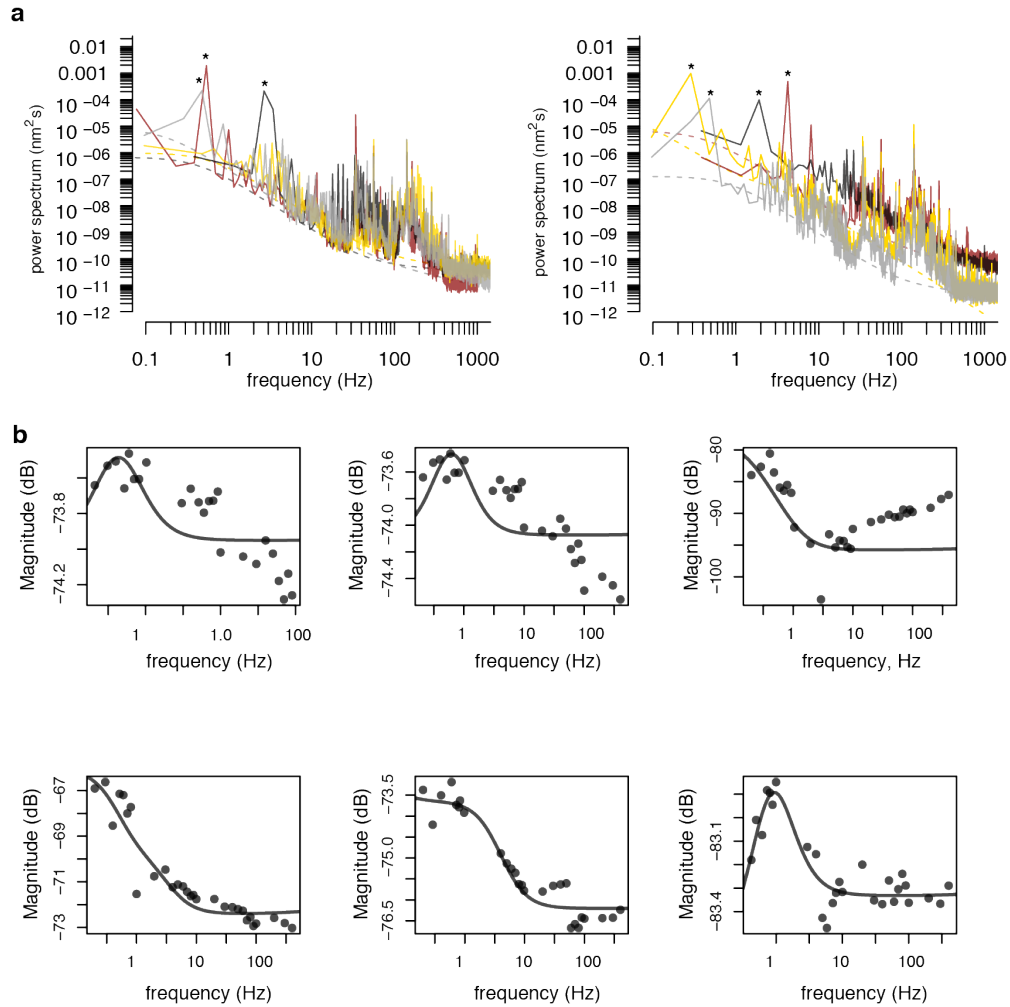
Figure S11 | Dynamic mechanical analysis of cytosol with optical tweezers. We measured the viscoelastic properties of the cytosol using the response of 200 nm polystyrene beads to sinusoidal oscillations of the tweezers and the high frequency domain of the power spectrum associated with thermal motions of the bead. (a) Power spectra of samples coded with distinct colors. Below frequencies of 500 Hz, the power spectra show fluctuations from tweezer oscillations (marked *), cellular processes and sample vibration. (b) Magnitude of the response (dB) of the bead displacement to sinusoidal oscillations of the optical trap position. Lines indicate global fits of the power spectra and response magnitudes to a model that describes the viscoelasticity of a crosslinked polymer network (Supplementary methods).
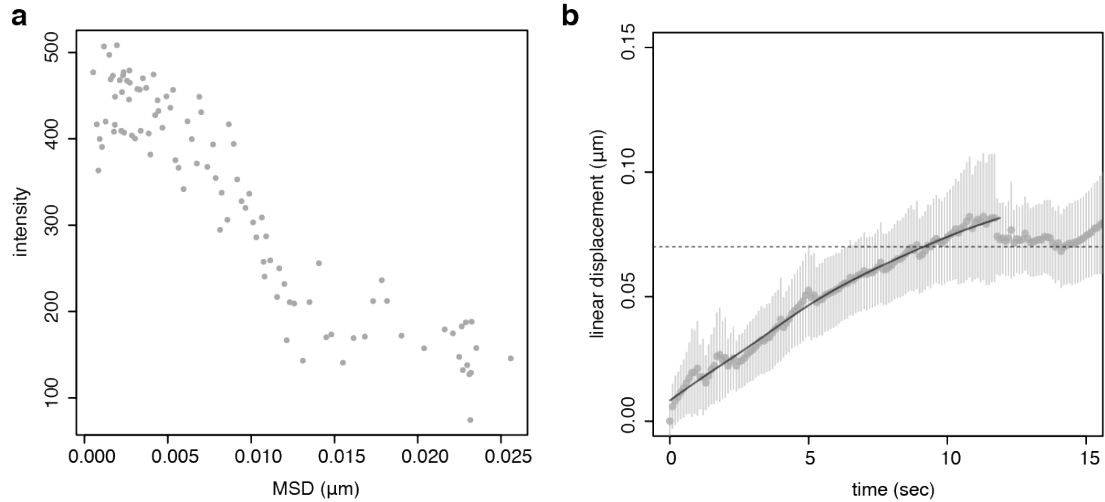
Figure S12 | Centroid tracking within a confocal volume of Sla1-GFP foci in *GPD1Δ* mutant strains treated with LatA. (a) Single Sla1-GFP focus fluorescence intensity as a function of mean square displacement in a confocal volume as determine by spinning disk pinhole size. Images were acquired at 10 frames per second. Only foci with a decreasing fluorescence bleaching were selected to measure their displacement. (b) Linear displacement of Sla1 foci within a confocal volume as a function of time. Mean ± sd of displacement is shown for n > 50 per time point. Total traces n = 275; note that traces do not have the same length. The average displacement is about 7.4 nm per second from polynomial fit (black curve). Horizontal dashed line indicates an invagination of 70 nm, depth required for the scission step.
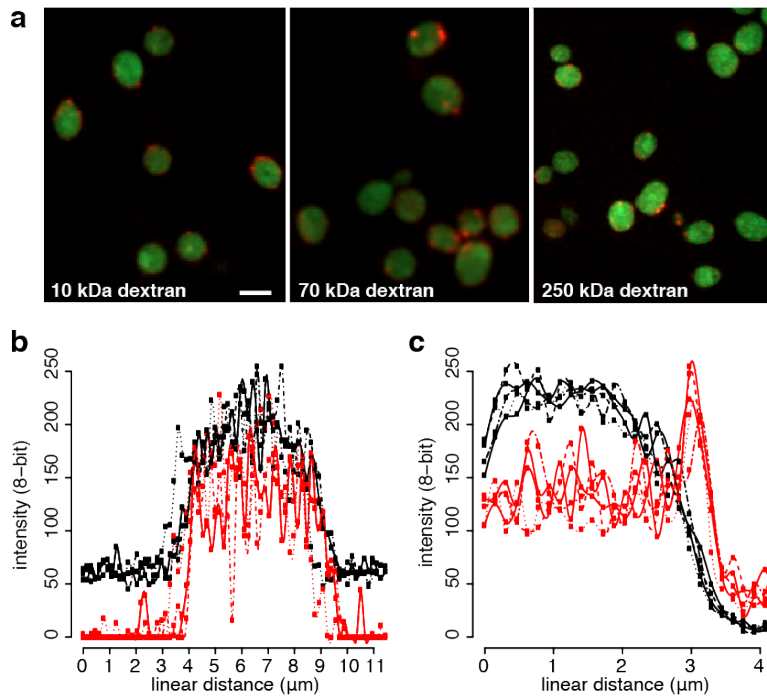
Figure S13 | Colocalization of different sized dextran-FITC revealed that cortical droplets exclude objects of diameters > 5.8 nm. (a) 2-color fluorescent images of osmoporated dextran-FITC of different sizes in a Sla1-mCherry strain, Scale bar is 4 μm. (b) Multiple line scans of osmoporated 70 kDa (5.8 nm) dextran-FITC fluorescent signal (back traces) outside Sla1-mCherry cortical regions (red traces). Fluorescence intensity patterns thus show the fluorescence of a line across the cytoplasm that doesn't include any concentrated foci of Sla1-mCherry. (c) Multiple line scans of osmoporated 70 kDa (5.8 nm) dextran-FITC fluorescent signal (back traces) within Sla1-mCherry cortical regions (red traces).

34

a
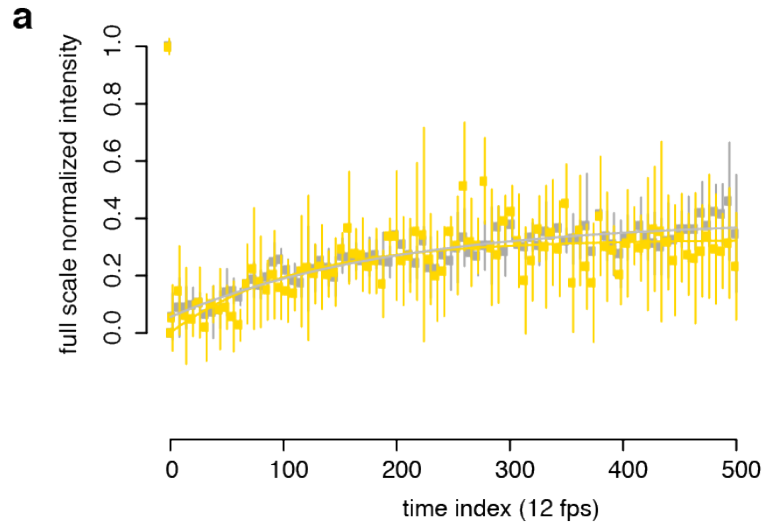
b

dextran-FITC	10 kDa	70 kDa	250 kDa
size	2.4 nm	5.8 nm	10.4 nm
bleach depth	0.75	0.80	0.79
mobile fraction in droplet	0.36	0.38	0.02

Figure S14 | Fluorescence recovery after photobleaching (FRAP) of dextran within cortical droplets or cytosol regions of interest. (a) FRAP of the bleached 2.4 nm (10 kDa) dextran-FITC within the Sla1 foci (yellow) and neighbouring cytosol regions (grey) without Sla1 signal. Images before and after FRAP. Data points represent mean normalized fluorescence of 3 independent samples. (b) Summary of FRAP analyzed for 2.4 nm, 5.8 nm and 10.4 nm dextran-FITC in the cortical droplet Sla1-mCherry region. Data shows absence of mobile fraction for the 10.4 nm dextran-FITC.
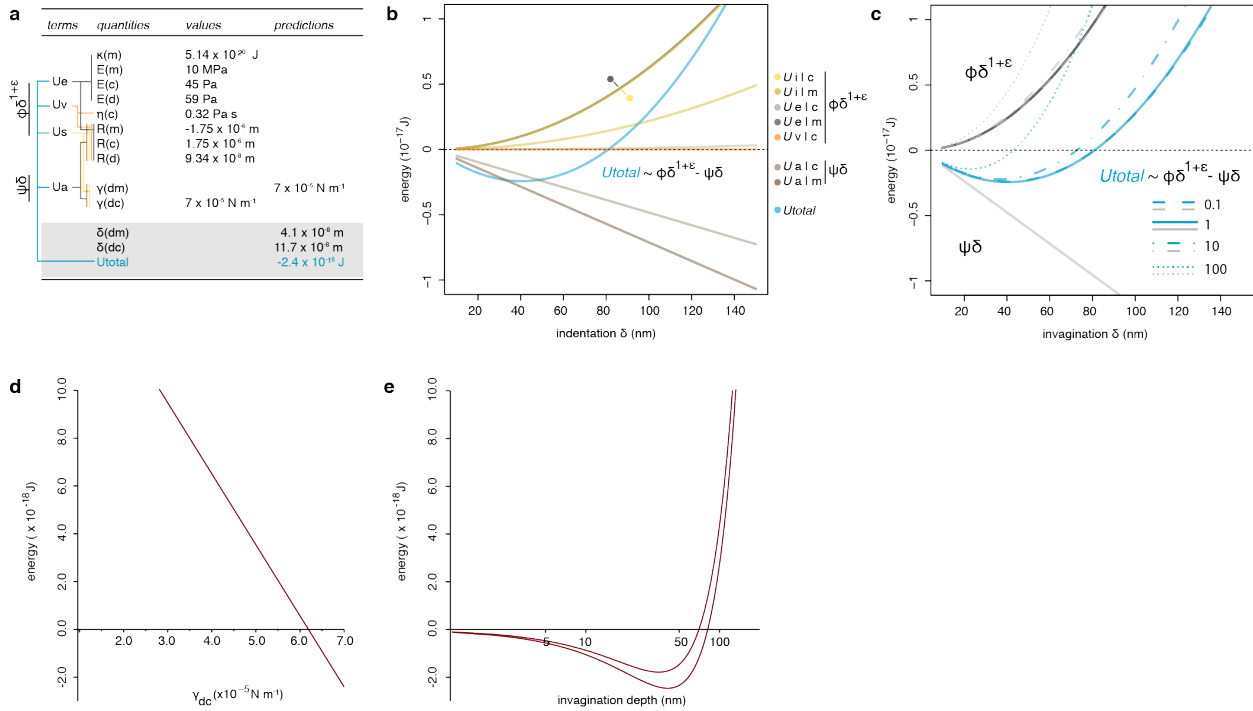
Figure S15 | Cortical droplets apply mechanical stress that deform the membrane. (a) Values of bending, elastic, viscosity, surface tension and geometry quantities used in the calculation are recapitulated. Colour coded lines indicate which quantities were used to calculated the respective energies U_x, that in turn compose the ϕ and ψ terms of Equation 1. (b) Equation (1) (insert) was used to calculate the energy penalties and contributions at the cytosol and membrane interfaces with the cortical droplet. Total energy of the system (blue), energy penalties (yellow, orange and grey) and energy contributions (brown) are presented as a function of membrane invagination (δ). Colour legend (right) specifies energy traces $U_{x|y}$, where x= (e), elasticity or (v), viscosity of either the cytosol (*c*) or membrane (*m*) and (i) is interfacial tension and (a) is adhesion of cytosol or membrane with the cortical droplet. Quantities used to calculate energies are detailed in Supplementary Tables 3 and 4. (c) Plot of total energy (y axis) as a function of droplet-cytosol surface tension (x axis) shows that the energy favorable values of γ_{dc} range between 6.2 x10^{-5} N•m^{-1} to 7 x10^{-5} N•m^{-1}. (d) 2D representation of the energy and depth accessible to a successful invagination. With the minimal (top curve) and maximal (lower curve) values of γ_{dm} our model predicts precise range of favorable δ (x axis) that minimizes total energy (y axis).

Supplementary Tables:

Table S1 | Strains used in this study

name	genotype	source
BY4741	MATa his3Δ1 leu2Δ0 met15Δ0 ura3Δ0	this study
GPD1Δ	4741 gpd1Δ::KanMX	YKO
SLA1Δ	4741 sla1Δ::KanMX	YKO
ENT1Δ	4741 ent1Δ::KanMX	YKO
ENT2Δ	4741 ent2Δ::KanMX	YKOs
LPS1Δ	4741 lps1Δ::KanMX	YKO
RGD1Δ	4741 rgd1Δ::KanMX	YKO
RVS161Δ	4741 rvs161Δ::KanMX	YKO
RVS167Δ	4741 rvs167Δ::KanMX	YKO
GVP36 Δ	4741 gvp36Δ::KanMX	YKO
PIL1Δ	4741 pli1Δ::KanMX	YKO
SYP1Δ	4741 syp1Δ::KanMX	YKO
Sla1-PLDΔ	4741 sla1-PLDΔ-Venus::HygMX	this study
Ent1-PLDΔ	4741 ent1-PLDΔ-Venus::HygMX	this study
Ent2-PLDΔ	4741 ent2-PLDΔ-Venus::HygMX	this study
Yap1801-PLDΔ	4741 yap1801f-PLDΔ-Venus::HygMX	this study
Yap1802-PLDΔ	4741 yap1802-PLDΔ-Venus::HygMX	this study
Sla1-GFP	4741 sla1-GFP::His3MX	GFP
Sla1-venus	4741 sla1-Venus::HygMX	this study
Sla1-mCherry	4741 sla1-mCherry::HygMX	this study
Sla1-Dronpa	4741 sla1-Dronpa3::NatMX	this study
Sla2-GFP	4741 sla2-GFP::His3MX	GFP
Ent1-venus	4741 ent1-Venus::HygMX	this study
Ent2-venus	4741 ent2-Venus::HygMX	this study
Yap1801-venus	4741 yap1801-Venus::HygMX	this study
Yap1802-venus	4741 yap1802-Venus::HygMX	this study
Sla1-mCherry Sla2-GFP	4741 sla2-GFP::His3MX sla1-mCherry::HygMX	this study
Sla1-GFP Sla2- mCherry	4741 sla1-GFP::His3MX sla2-mCherry::HygMX	this study

name	genotype	source
Lps1-GFP Sla1-mCherry	4741 lps1-GFP::His3MX sla1-mCherry::HygMX	this study
Rgd1-GFP Sla1-mCherry	4741 rgd1-GFP::His3MX sla1-mCherry::HygMX	this study
Rvs161-GFP Sla1-mCherry	4741 rvs161-GFP::His3MX sla1-mCherry::HygMX	this study
Rvs167-GFP Sla1-mCherry	4741 rvs167-GFP::His3MX sla1-mCherry::HygMX	this study
Gvp36-GFP Sla1-mCherry	4741 gvp36-GFP::His3MX sla1-mCherry::HygMX	this study
Pil1-GFP Sla1-mCherry	4741 pil1-GFP::His3MX sla1-mCherry::HygMX	this study
Syp1-GFP Sla1-mCherry	4741 syp1-GFP::His3MX sla1-mCherry::HygMX	this study
Lps1-GFP Sac6-mCherry	4741 lps1-GFP::His3MX sac6-mCherry::HygMX	this study
Rgd1-GFP Sac61-mCherry	4741 rgd1-GFP::His3MX sac6-mCherry::HygMX	this study
Rvs161-GFP Sac6-mCherry	4741 rvs161-GFP::His3MX sac6-mCherry::HygMX	this study
Rvs167-GFP Sac6-mCherry	4741 rvs167-GFP::His3MX sac6-mCherry::HygMX	this study
Gvp36-GFP Sac6-mCherry	4741 gvp36-GFP::His3MX sac6-mCherry::HygMX	this study
Pil1-GFP Sac6-mCherry	4741 pil1-GFP::His3MX sac6-mCherry::HygMX	this study
Syp1-GFP Sac6-mCherry	4741 syp1-GFP::His3MX sac6-mCherry::HygMX	this study

Table S2 | Parameters and variables used in our model were either measured in this study or obtained from the literature

parameters	definition	value	note	source
E_m	membrane elastic modulus	1×10^7 Pa	*estimate*	Landau 1986
κ_m	membrane bending modulus	$12.5 \cdot K_B T$		Harmandaris 2006
v_m	membrane poisson's ratio	0.45	*from 0.1 to 0.5*	Zhang 2013
δ_m	membrane indentation	5×10^{-8} m	from 2.5×10^{-8} to 5×10^{-8} m	EM
R_m	membrane radius	-1.75×10^{-6} m	*negative curvature*	*this study*
E_c	cytosol elastic modulus	45 Pa	at 1 Hz	*this study*
η	cytosol viscosity	0.35 Pa·s^{-1}	*at 0.5 Hz*	*this study*
v_c	cytoplasm poisson's ratio	0.45	*from 0.1 to 0.5*	Zhang 2013
δ_c	indentation cytosol	1.18×10^{-7} m	$\pm 6 \times 10^{-9}$ m	*this study*
R_c	membrane radius	1.75×10^{-6} m		*this study*
E_{drop}	droplet elastic modulus	59 Pa		*this study*
$2a_{drop}$	droplet contact diameter	2.09×10^{-7} m	$\pm 1 \times 10^{-8}$ m	*this study*
δ_{drop}	indentation droplet	1.18×10^{-7} m	$\pm 6 \times 10^{-9}$ m	*this study*
R_{drop}	droplet radius	9.3×10^{-7} m	$\sim a^2/R$	*Hertz*
θ	droplet contact angle	96.7°	$\theta = 2 \arctan(\delta_{drop}/a_{drop})$	Young

* EM refers to electron microscopy data from (Kukulski, Picco et al. 2016) and Hertz refers to Hertz contact theory (Hertz 1882). Landau 1986 refers to estimation of membrane elastic modulus from the bending modulus and Poisson's ratio (Landau, Lifshits et al. 1986), Harmandaris 2006 (Harmandaris and Deserno 2006) and Zhang 2013 (Zhang, Soman et al. 2013).

Table S3 | Constants and equations used in the elasto-adhesion model for the deformation of the membrane by protein droplets on cortical sites

variables	definition	value	note	source
mechanical stress method				
$\dot{\varepsilon}$	cytosol deformation rate	0.004 s^{-1}		
E_{cell}	cell apparent elastic modulus	1000 Pa		AFM
σ	mechanical stress	1181Pa	$\sigma = \varepsilon E + \varepsilon \eta$	Kelvin-Voigt
ΔP	pressure difference	1181Pa	$\Delta P = \sigma$	Laplace
H	interface mean curvature	$8.5 \times 10^6 \text{ m}^{-1}$	$1/R$	Laplace
γ_{dc}	droplet-cytoplasm surface tension	$7 \times 10^{-5} \text{N} \cdot \text{m}^{-1}$	$\gamma = \Delta P / (2H)$	Young-Laplace
elasto-adhesive contact method				
c	constant	0.92	$8/(5\sqrt{3})$	JKR
E^*_{dc}	cytoplasmic interface equivalent elastic modulus	32 Pa	$1/E^*_c = (1-v_c^2)/E_c + (1-v_m^2)/E_m$	Hertz
E^*_{dm}	membrane interface equivalent elastic modulus	75 Pa		Hertz
R_{dm}	equivalent radius	$1.27 \times 10^{-7} \text{ m}$	$1/R = 1/R_m + 1/R_d$	Hertz
R_{dc}	equivalent radius	$1.11 \times 10^{-7} \text{ m}$	$1/R = 1/R_c + 1/R_d$	Hertz
δ_c	cytoplasm indentation	*see table S3*	$f(\delta_m) = \mu + \omega \delta_m$	*this study*
μ	constant	1.65		*this study*
k	constant	0		*this study*
W_{dm}	droplet-membrane work of adhesion	$6.15 \times 10^{-5} \text{ N} \cdot \text{m}^{-1}$	$W_{dm} = \gamma_{dc}(1+\cos\theta)$	Young-Dupré

variables	definition	value	note	source
W_{dc}	droplet-cytosol work of adhesion	6.15×10^{-5} N•m^{-1}	$= \gamma_{cm} + \gamma_{dm} - \gamma_{dc}$ predicted from model *(1 x 10^{-5} to 7 x10^{-5}N•m^{-1})*	*this study*
γ_{dm}	droplet-membrane surface tension	6.15×10^{-5} N•m^{-1}	$\gamma_{dm} < \gamma_{dc}$ *(hydrophobic)* $\gamma_{dm} \sim (W_{dc} + \gamma_{dc})/2$	Young-Dupré
γ_{cm}	cytosol-membrane surface tension	5.75×10^{-5} N•m^{-1}	$\gamma_{cm} = \gamma_{dm} + (\gamma_{dc}\cos\theta)$	Young

* not determined (nd). AFM refers to atomic force microscopy data from (Munder, Midtvedt et al. 2016).

Table S4 | Summary of the indentations and energies predicted with our elasto-adhesive contact model

variable	definition	value	in kT	source
δ_m	membrane indentation	4.06×10^{-8} m	*nd*	*this study*
δ_c	cytoplasm indentation	1.17×10^{-7} m	*nd*	*this study*
U_{total}	total energy of system	-2.4×10^{-18} J	*-590·kT*	*this study*
U_{penal}	total energy penalties	2.4×10^{-18} J	*590·kT*	*this study*
U_{em}	corrected elastic energy at membrane interface	1×10^{-18} J	*250·kT*	*this study*
U_{ec}	elastic energy at cytoplasm interface	1.2×10^{-20} J	*3·kT*	*this study*
$U_{\gamma m}$	surface energy at membrane interface	3.6×10^{-19} J	*88·kT*	*this study*
$U_{\gamma c}$	surface energy at cytoplasm interface	1×10^{-18} J	*249·kT*	*this study*
U_{vc}	viscous friction energy	2.5×10^{-21} J	*1·kT*	*this study*
U_{adh}	total adhesion energy	4.9×10^{-18} J	*1180·kT*	*this study*
U_{am}	adhesion energy at membrane interface	2×10^{-18} J	*477·kT*	*this study*
U_{ac}	adhesion energy at cytoplasm interface	2.9×10^{18} J	*703·kT*	*this study*

Supplementary movies:

Movie S1 | pulse-chase experiments with HD showed that HD-dependent dissolution of Sla1 puncta was reversible

References:

1. Avinoam, O., M. Schorb, C. J. Beese, J. A. Briggs and M. Kaksonen (2015). "ENDOCYTOSIS. Endocytic sites mature by continuous bending and remodeling of the clathrin coat." <u>Science</u> **348** (6241): 1369-1372.
2. Boettner, D. R., J. L. D'Agostino, O. T. Torres, K. Daugherty-Clarke, A. Uygur, A. Reider, B. Wendland, S. K. Lemmon and B. L. Goode (2009). "The F-BAR protein Syp1 negatively regulates WASp-Arp2/3 complex activity during endocytic patch formation." <u>Curr Biol</u> **19** (23): 1979-1987.
3. Brangwynne, C. P., T. J. Mitchison and A. A. Hyman (2011). "Active liquid-like behavior of nucleoli determines their size and shape in Xenopus laevis oocytes." <u>Proc Natl Acad Sci U S A</u> **108** (11): 4334-4339.
4. Busch, D. J., J. R. Houser, C. C. Hayden, M. B. Sherman, E. M. Lafer and J. C. Stachowiak (2015). "Intrinsically disordered proteins drive membrane curvature." <u>Nat Commun</u> **6**: 7875.
5. Carlsson, A. E. and P. V. Bayly (2014). "Force generation by endocytic actin patches in budding yeast." <u>Biophys J</u> **106** (8): 1596-1606.
6. da Silva Pedrini, M. R., S. Dupont, A. de Anchieta Camara, Jr., L. Beney and P. Gervais (2014). "Osmoporation: a simple way to internalize hydrophilic molecules into yeast." <u>Appl Microbiol Biotechnol</u> **98** (3): 1271-1280.
7. Derganc, J. and A. Copic (2016). "Membrane bending by protein crowding is affected by protein lateral confinement." <u>Biochim Biophys Acta</u> **1858** (6): 1152-1159.
8. Dill, K. A. and S. Bromberg (2011). <u>Molecular driving forces : statistical thermodynamics in biology, chemistry, physics, and nanoscience</u>. London ; New York, Garland Science.
9. Ford, M. G., I. G. Mills, B. J. Peter, Y. Vallis, G. J. Praefcke, P. R. Evans and H. T. McMahon (2002). "Curvature of clathrin-coated pits driven by epsin." <u>Nature</u> **419** (6905): 361-366.
10. French, J. B., H. Zhao, S. An, S. Niessen, Y. Deng, B. F. Cravatt and S. J. Benkovic (2013). "Hsp70/Hsp90 chaperone machinery is involved in the assembly of the purinosome." <u>Proceedings of the National Academy of Sciences</u> **110** (7): 2528-2533.
11. Gleisner, M., B. Kroppen, C. Fricke, N. Teske, T. T. Kliesch, A. Janshoff, M. Meinecke and C. Steinem (2016). "Epsin N-terminal Homology Domain (ENTH) Activity as a Function of Membrane Tension." <u>J Biol Chem</u> **291** (38): 19953-19961.
12. Harmandaris, V. A. and M. Deserno (2006). "A novel method for measuring the bending rigidity of model lipid membranes by simulating tethers." <u>J Chem Phys</u> **125** (20): 204905.
13. Helfrich, W. (1973). "Elastic properties of lipid bilayers: theory and possible experiments." <u>Z Naturforsch C</u> **28** (11): 693-703.
14. Hendricks, A. G., E. L. Holzbaur and Y. E. Goldman (2012). "Force measurements on cargoes in living cells reveal collective dynamics of microtubule motors." <u>Proc Natl Acad Sci U S A</u> **109** (45): 18447-18452.
15. Hertz, H. R. (1882). <u>Ueber die Beruehrung elastischer Koerper (On Contact Between Elastic Bodies)</u>. Leipzig, Germany, 1895.
16. Ho, C. H., L. Magtanong, S. L. Barker, D. Gresham, S. Nishimura, P. Natarajan, J. L. Koh, J. Porter, C. A. Gray, R. J. Andersen, G. Giaever, C. Nislow, B. Andrews, D. Botstein, T. R. Graham, M. Yoshida and C. Boone (2009). "A molecular barcoded yeast ORF library enables mode-of-action analysis of bioactive compounds." <u>Nat Biotechnol</u> **27** (4): 369-377.
17. Huh, W. K., J. V. Falvo, L. C. Gerke, A. S. Carroll, R. W. Howson, J. S. Weissman and E. K. O'Shea (2003). "Global analysis of protein localization in budding yeast." <u>Nature</u> **425** (6959): 686-691.
18. Idrissi, F. Z., A. Blasco, A. Espinal and M. I. Geli (2012). "Ultrastructural dynamics of proteins involved in endocytic budding." <u>Proc Natl Acad Sci U S A</u> **109** (39): E2587-2594.
19. Idrissi, F. Z., H. Grotsch, I. M. Fernandez-Golbano, C. Presciatto-Baschong, H. Riezman and M. I. Geli (2008). "Distinct acto/myosin-I structures associate with endocytic profiles at the plasma membrane." <u>J Cell Biol</u> **180** (6): 1219-1232.
20. Kanshin, E., L. P. Bergeron-Sandoval, S. S. Isik, P. Thibault and S. W. Michnick (2015). "A cell-signaling network temporally resolves specific versus promiscuous phosphorylation." <u>Cell Rep</u> **10** (7): 1202-1214.
21. Koenderink, G. H., M. Atakhorrami, F. C. MacKintosh and C. F. Schmidt (2006). "High-frequency stress relaxation in semiflexible polymer solutions and networks." <u>Phys Rev Lett</u> **96** (13): 138307.
22. Kroschwald, S., S. Maharana, D. Mateju, L. Malinovska, E. Nuske, I. Poser, D. Richter and S. Alberti (2015). "Promiscuous interactions and protein disaggregases determine the material state of stress-inducible RNP granules." <u>Elife</u> **4**: e06807.

23. Kukulski, W., A. Picco, T. Specht, J. A. Briggs and M. Kaksonen (2016). "Clathrin modulates vesicle scission, but not invagination shape, in yeast endocytosis." Elife **5**.
24. Kukulski, W., M. Schorb, M. Kaksonen and J. A. Briggs (2012). "Plasma membrane reshaping during endocytosis is revealed by time-resolved electron tomography." Cell **150** (3): 508-520.
25. Landau, L. D., E. M. Lifshits, A. d. M. Kosevich and L. P. Pitaevskiæi (1986). Theory of elasticity. Oxford ; New York, Pergamon Press.
26. Lieleg, O., K. M. Schmoller, M. M. Claessens and A. R. Bausch (2009). "Cytoskeletal polymer networks: viscoelastic properties are determined by the microscopic interaction potential of cross-links." Biophys J **96** (11): 4725-4732.
27. Munder, M. C., D. Midtvedt, T. Franzmann, E. Nuske, O. Otto, M. Herbig, E. Ulbricht, P. Muller, A. Taubenberger, S. Maharana, L. Malinovska, D. Richter, J. Guck, V. Zaburdaev and S. Alberti (2016). "A pH-driven transition of the cytoplasm from a fluid- to a solid-like state promotes entry into dormancy." Elife **5**.
28. Picco, A., M. Mund, J. Ries, F. Nedelec and M. Kaksonen (2015). "Visualizing the functional architecture of the endocytic machinery." Elife **4**.
29. Reiter, W., D. Anrather, I. Dohnal, P. Pichler, J. Veis, M. Grotli, F. Posas and G. Ammerer (2012). "Validation of regulated protein phosphorylation events in yeast by quantitative mass spectrometry analysis of purified proteins." Proteomics **12** (19-20): 3030-3043.
30. Roman, B. and J. Bico (2010). "Elasto-capillarity: deforming an elastic structure with a liquid droplet." J Phys Condens Matter **22** (49): 493101.
31. Sheff, M. A. and K. S. Thorn (2004). "Optimized cassettes for fluorescent protein tagging in Saccharomyces cerevisiae." Yeast **21** (8): 661-670.
32. Style, R. W., C. Hyland, R. Boltyanskiy, J. S. Wettlaufer and E. R. Dufresne (2013). "Surface tension and contact with soft elastic solids." Nat Commun **4**: 2728.
33. Tarassov, K., V. Messier, C. R. Landry, S. Radinovic, M. M. Serna Molina, I. Shames, Y. Malitskaya, J. Vogel, H. Bussey and S. W. Michnick (2008). "An in vivo map of the yeast protein interactome." Science **320** (5882): 1465-1470.
34. Youn, J. Y., H. Friesen, T. Kishimoto, W. M. Henne, C. F. Kurat, W. Ye, D. F. Ceccarelli, F. Sicheri, S. D. Kohlwein, H. T. McMahon and B. J. Andrews (2010). "Dissecting BAR domain function in the yeast Amphiphysins Rvs161 and Rvs167 during endocytosis." Mol Biol Cell **21** (17): 3054-3069.
35. Zhang, W., P. Soman, K. Meggs, X. Qu and S. Chen (2013). "Tuning the Poisson's Ratio of Biomaterials for Investigating Cellular Response." Adv Funct Mater **23** (25): 3226-3232.